Published in final edited form as:
Nat Med. 2018 June ; 24(6): 834–846. doi:10.1038/s41591-018-0035-5.

Elevated prenatal anti-Müllerian hormone reprograms the fetus and induces polycystic ovary syndrome in adulthood

Brooke Tata[#1,2], **Nour El Houda Mimouni**[#1,2], **Anne-Laure Barbotin**[1,3], **Samuel A. Malone**[1,2], **Anne Loyens**[1,2], **Pascal Pigny**[2,4], **Didier Dewailly**[1,2,5], **Sophie Catteau-Jonard**[1,2,5], **Inger Sundström-Poromaa**[6], **Terhi T. Piltonen**[7], **Federica Dal Bello**[8], **Claudio Medana**[8], **Vincent Prevot**[1,2], **Jerome Clasadonte**[1,2,10], and **Paolo Giacobini**[1,2,10,*]

[1]Jean-Pierre Aubert Research Center (JPArc), Laboratory of Development and Plasticity of the Neuroendocrine Brain, Inserm, UMR-S 1172, Lille, France [2]University of Lille, FHU 1,000 Days for Health, Lille, France [3]CHU Lille, Institut de Biologie de la Reproduction-Spermiologie-CECOS, Lille, France [4]CHU Lille, Laboratoire de Biochimie & Hormonologie, Centre de Biologie Pathologie, Lille, France [5]CHU Lille, Service de Gynécologie Endocrinienne et Médecine de la Reproduction, Hôpital Jeanne de Flandre, Lille, France [6]Department of Women's and Children's Health, Uppsala University, Uppsala, Sweden [7]Department of Obstetrics and Gynecology, Oulu University Hospital, Oulu, Finland; University of Oulu and Medical Research Center Oulu, Oulu, Finland [8]Department of Molecular Biotechnology and Health Science, University of Torino, Torino, Italy

[#] These authors contributed equally to this work.

Abstract

Polycystic ovary syndrome (PCOS) is the main cause of female infertility worldwide and corresponds with a high degree of comorbidities and economic burden. How PCOS is passed on from one generation to the next is not clear, but it may be a developmental condition. Most women with PCOS exhibit higher levels of circulating luteinizing hormone, suggestive of heightened gonadotropin-releasing hormone (GnRH) release, and Anti-Müllerian Hormone (AMH) as

[*]Correspondence should be addressed to Paolo Giacobini (paolo.giacobini@inserm.fr).
[10]The authors co-supervised this work

Life Sciences Reporting Summary
Further information on experimental design is available in the Life Sciences Reporting Summary.

Data Availability
The data supporting the findings of the current study are available from the corresponding author upon request.

Author Contributions
P.G. designed the study, analyzed data, prepared the figures and wrote the manuscript. J.C. performed electrophysiological recordings and was involved in all aspects of study design, interpretation of results and manuscript preparation; B.T., N.E.H.M., A.-L.B., designed and performed the experiments and analyzed the data; A.L., assisted with experiments; P.P. performed the AMH measurements in blood human samples; S.A.M. performed tissue-clearing experiments; D.D., S.C.-J., T.T.P., helped on several aspects of interpretation of clinical and preclinical results and manuscript preparation; I.S.-P. provided biological samples and clinical information for the human study; C.M and F.D.B. performed nano-HPLC-HRMS experiments; V.P. was involved in the study design, interpretation of the results and preparation of the manuscript.

Competing Financial Interests
The authors have no financial competing interests.

Europe PMC Funders Author Manuscripts

compared to healthy women. Excess AMH *in utero* may affect the development of the female fetus. However, as AMH levels drop during pregnancy in women with normal fertility it was unclear if their levels were also elevated in pregnant women with PCOS. Here, we measured AMH in a cohort of pregnant women with PCOS and control women and found that AMH is significantly more elevated in the former group versus the latter. To determine if the elevation of AMH during pregnancy in women with PCOS is a bystander effect or a driver of the condition in the offspring, we modelled our clinical findings by treating pregnant mice with AMH and followed the neuroendocrine phenotype of their female progeny postnatally. This treatment resulted in maternal neuroendocrine-driven testosterone excess and diminished placental metabolism of testosterone to estradiol, resulting in a masculinization of the exposed female fetus and a PCOS-like reproductive and neuroendocrine phenotype in adulthood. We found that the affected females had persistently hyperactivated GnRH neurons and that GnRH antagonist treatment in the adult female offspring restored their neuroendocrine phenotype to a normal state. These findings highlight a critical role for excess prenatal AMH exposure and subsequent aberrant GnRH receptor signaling in the neuroendocrine dysfunctions of PCOS, while offering a new potential therapeutic avenue to treat the condition during adulthood.

Keywords

AMH; GnRH; PCOS; fetal programming; aromatase; PAMH

PCOS is the most common female reproductive disorder, affecting 10-18% of women of reproductive age worldwide1–4. The syndrome is underpinned by excessive ovarian and/or adrenal androgen secretion, oligo-anovulation and, in many cases, insulin resistance and associated metabolic derangements2,5,6. In non-pregnant women with PCOS, serum levels of AMH are 2-3–fold higher than in women without polycystic ovaries (PCO) or PCOS7,8 and the severity of the reproductive dysfunction is positively correlated with AMH levels9,10. The pathophysiology of PCOS also extends to hypothalamic neuronal dysregulation as most PCOS individuals exhibit increased luteinizing hormone (LH) levels suggestive of high-frequency GnRH secretion2,11,12. Whether this defect is primary or secondary to other changes in PCOS remains unclear but recent evidence has shown that GnRH-positive neurons express AMH receptors and that exogenous AMH potently increases GnRH neuron firing and GnRH release in murine living tissue explants11.

Familial clustering and twin studies have shown that PCOS has a strong heritable component13. However, the mutations that have been identified so far do not account for its high prevalence in the population, implying that fetal environmental factors might play important roles in the onset of this disease14.

Here, we showed that AMH concentrations during pregnancy are significantly higher in women with PCOS as compared to women with no reproductive defects. Using mouse models, we showed that exposure to excess AMH during gestation engages a series of events in the dams leading to a fetal programming of the exposed offspring into exhibiting a PCOS-like reproductive and neuroendocrine phenotype in adulthood. GnRH antagonist treatment of these offspring during adulthood normalizes their neuroendocrine phenotype.

Results

AMH levels during pregnancy are higher in women with PCOS than in controls

AMH levels were previously found to be low during pregnancy in women with normal fertility15,16; however, whether this is the case also for pregnant women with PCOS has never been investigated. Here, we examined AMH levels in a cohort of 63 control pregnant women and 66 subjects with PCOS, at gestational week 16-19 (Fig. 1a). This analysis revealed significant differences in AMH median values between the two populations, with AMH being higher in pregnant PCOS subjects than in control women (Fig. 1b). This was not attributable to differences in age between the two groups (Supplementary Table 1). When we analyzed this sample stratified by body mass index (BMI), and classified women as lean or obese (lean BMI $\leq$25 kg/m^2, obese BMI $\geq$30 kg/m^2), we found that AMH was significantly higher in pregnant lean women with PCOS compared with the control group but not in obese subjects with PCOS versus obese control individuals (Fig. 1c). We subsequently analyzed the AMH values within the cohort of pregnant subjects with PCOS taking into account BMI and hyperandrogenism (normoandrogenic vs. hyperandrogenic, the latter defined as either biochemical or clinical hyperandrogenism). We detected a significant difference between lean normo- and hyperandrogenic individuals with PCOS, with AMH being more elevated in hyperandrogenic lean women with PCOS than in normoandrogenic women (Fig. 1d). No difference between normo- and hyperandrogenic obese women with PCOS was detected (Fig. 1d). Finally, we analyzed the control and PCOS groups stratified by age (age 27-34 years and age > 34 years), and found higher AMH levels in both PCOS age groups compared with their respective control women (Fig. 1e).

Prenatal AMH-treatment triggers the neuroendocrine disturbances of PCOS in the offspring

To test whether prenatal exposure to elevated AMH might lead to PCOS later in life, we treated pregnant female mice with PBS or recombinant AMH at the end of gestation and studied the neuroendocrine reproductive features of the female offspring at adulthood (Fig. 2a).

Pregnant mice were injected intraperitoneally (i.p.) with 0.01 M phosphate buffered saline, pH 7.4 (PBS, Control) or with the bioactive form of AMH (human recombinant AMH_C, 0.12 mg/Kg/day; prenatal AMH_C-treated, PAMH)11 during the same temporal window (E16.5-E18.5) that was previously used to generate prenatal androgen-treated mice, PNA17–19 (Fig. 2a). We chose this temporal window for the treatment because it lies beyond the developmental stages during which gonadal and genital tract differentiation takes place in mice (E12.5-E14.5), which therefore excludes any morphogenetic effects that exogenous AMH could have20. PAMH offspring exhibited delayed vaginal opening (VO), delayed puberty onset (Supplementary Fig. 1a, b), severely disrupted estrous cyclicity (oligo-anovulation; Fig. 2b, c) and no difference in body weight (Supplementary Fig. 1d). PAMH mice rarely entered the preovulatory stage of the estrous cycle and displayed prolonged time in metestrus/diestrus as compared to the control female offspring (Fig. 2b, c; metestrus/diestrus: M/D, estrus: E, proestrus: P). Ovarian histology of PAMH animals showed abnormalities consistent with their anovulatory phenotype, with the presence of fewer post-

ovulation corpora lutea and less late antral follicles as compared to control animals (Fig. 2d). In addition, PAMH adult female mice also showed impaired fertility as indicated by a significant delay in their first litter, fewer litters and fewer pups per litter produced over a 3-month period (Fig. 2e).

To test whether this disruptive effect of prenatal AMH treatment is eventually mediated by GnRH binding to the GnRH receptor, we treated pregnant mice with AMH_C along with a GnRH antagonist, at a concentration previously validated in animal works (Cetrorelix acetate, 0.5 mg/Kg/day)11, from E16.5 to E18.5. Cetrorelix is known to specifically saturate GnRH receptors at the level of the anterior pituitary21,22 thus decreasing the GnRH-mediated release of LH and Follicle Stimulating Hormone (FSH), with an effect more pronounced on LH secretion 23. Prenatal GnRH antagonist treatment prevented the appearance of reproductive defects in postnatal offspring (PAMH + GnRH antag; Fig. 2b,e). To determine whether AMH treatment affects the levels of circulating testosterone (T) in PAMH animals, we measured the ano-genital distance, which reflects androgenic impregnation, from postnatal day 30 (P30) to P60 (Fig. 3a). The PAMH female offspring displayed a significantly longer ano-genital distance than control female offspring (Fig. 3a). This phenotype was also completely reversed by the prenatal co-treatment of AMH with the GnRH antagonist (Fig. 3a). Accordingly, circulating T and LH levels, measured at diestrus, were markedly elevated in PAMH compared to control and PAMH+GnRH antagonist mice (Fig. 3b,c). We then evaluated LH pulsatility, by serial blood sampling, in female diestrous mice (Fig. 3d) and found that PAMH animals had a significantly higher LH pulse frequency as compared to control and AMH+GnRH antagonist treatment groups (Fig. 3e,f). This is suggestive of an alteration in the hypothalamic network activity of the offspring caused by late-gestational exposure to AMH excess.

These data show that the PAMH mouse model displays the major cardinal PCOS neuroendocrine features: hyperandrogenism, LH elevation, sporadic ovulation and fertility defects. However, PAMH animals did not present weight alterations, indicating that this model is most representative of the lean PCOS phenotype.

We also investigated whether prenatal exposure to the AMH precursor, proprotein (proAMH; 140 kDa) would recapitulate the same PCOS-like traits observed upon injection of the bioactive form of AMH (AMH_C; 23.4 kDa). We injected pregnant mice daily with PBS (Control) or with the proAMH (AMH, 0.12 mg/Kg/d) from E16.5 to E18.5. Phenotypic characterization of the offspring (Supplementary Fig. 1a-h) show that prenatal exposure to proAMH mirrors the PCOS neuroendocrine features observed in PAMH mice.

Peripherally administered AMH acts centrally by inducing GnRH neuronal activation

To test whether peripherally administered AMH could impinge on the maternal GnRH neurons leading to their activation, we quantified the number of active GnRH-positive neurons ($GnRH^+/Fos^+$) 90 minutes after i.p. delivery of AMH_C (Supplementary Fig. 2a-d). Indeed, a single AMH injection significantly increased the total number of Fos^+ nuclei in the hypothalamic OVLT (organum vasculosum laminae terminalis; Supplementary Fig. 2a-c) as well as the proportion of GnRH-positive neurons expressing Fos in the same regions (Supplementary Fig. 2a,b,d). Next, we studied whether blood-borne AMH could enter the

maternal brain and/or the fetal brain. For this purpose, we intravenously administered fluorescently-labeled bioactive AMH to E16.5 pregnant mice 2 min before sacrifice and subsequently harvested respectively the brains of the dams, the placentae and the heads of the embryos (Supplementary Fig. 2e-i). Fluorescent AMH was detectable in the maternal brains at the level of the ME, which lies outside the blood-brain-barrier (BBB), where it diffuses out of the fenestrated endothelial cells, into the external layer of the ME, and where GnRH terminals are located (Supplementary Fig. 2f). 3D analysis of fluorescent AMH in solvent-cleared intact placentae, collected from these animals, highlighted the presence of AMH in the maternal side but not in the fetal side of the placenta, indicating that AMH cannot cross the placental barrier (Supplementary Fig. 2h). This was confirmed by the lack of fluorescent AMH in the sections of the corresponding embryo brains (Supplementary Fig. 2i). We also verified whether Cetrorelix injected i.p. could access the maternal and, eventually, the embryo brain. Dams were treated either with PBS or Cetrorelix (0.5 mg/Kg/day) from E16.5 to E18.5; maternal and embryo brains were harvested one day later. High Pressure Liquid Chromatography–High Resolution Mass Spectrometry (Nano-HPLC-HRMS) analysis revealed the presence of Cetrorelix in the brains of the injected dams as well as in the embryo brains (Supplementary Fig. 3a,b).

Peripheral AMH causes gestational hyperandrogenism through a brain-ovarian-placental crosstalk

Since LH secretion is an indirect measurement of GnRH neuronal secretion, we measured LH in pregnant mice one day after vehicle (PBS), AMH or AMH + GnRH antagonist treatment (E19.5; Fig. 3g). During pregnancy serum LH levels are known to be almost undetectable as a consequence of the progesterone brake. Circulating LH levels were found to be 5 times higher in AMH-treated pregnant mice as compared to the control group (Fig. 3g), while this increase was prevented by the prenatal co-treatment of AMH with the GnRH antagonist (Fig. 3g). AMH-treated pregnant females also showed significantly higher T compared to control and AMH + GnRH antag dams, which displayed very low T levels (Fig. 3g). We next measured circulating estradiol (E2) and progesterone (P) in those treatment groups and found lower levels of both hormones in the AMH-treated dams as compared to the vehicle-treated and AMH + GnRH antag-treated dams (Fig. 3g). These data indicate that late gestational exposure to high AMH is sufficient to generate in dams heightened LH and T levels and diminished E2 and P concentrations in a GnRH-dependent manner.

Since the placenta expresses AMHR2 both in humans24 and in mice (Fig. 3h) and high T and low E2 levels were found in AMH-treated dams (Fig. 3g), we examined if AMH treatment could alter aromatase expression in the murine placenta, possibly affecting the conversion of T into E2. We performed qPCR for *Cyp19a1*, which encodes for the enzyme P450 aromatase, in the placentae harvested from pregnant mice at the end of the treatment period (Fig. 3h). AMH treatment significantly lowered *Cyp19a1* expression as compared to the other treatment groups (Fig. 3h). Since the GnRH antag treatment prevented the AMH-driven inhibition of *Cyp19a1* (Fig. 3h), we investigated the expression of *Gnrh1*, GnRH receptor (*Gnrhr*) and LH receptor (*Lhr*) transcripts in the placentae collected from those animals (Supplementary Fig. 4). All genes were found to be expressed in the placenta of the different treatment groups. While the expression of *Gnrh1* and *Gnrhr* was unchanged among

treatment groups, *Lhr* expression was found to be significantly higher in the AMH-treated dams compared to control dams and to AMH + GnRH antag-treated dams (Supplementary Fig. 4). We next quantified placental expression of *Cyp11a1* and *Hsd3b1*, two genes encoding for key steroidogenic enzymes involved in onset of steroidogenesis and derivation of progesterone, respectively. We did not find any difference in the expression of *Cyp11a1* among treatment groups but we found significantly lower *Hsd3b1* expression in the placentae of AMH-treated- versus control and AMH + GnRH antagonist-treated dams (Fig. 3h). These data show that GnRH antagonist treatment prevented the downregulation of *Hsd3b1* gene expression, indicating normalization of the GnRH/LH-driven maternal steroidogenesis.

As T is an anabolic hormone, we monitored whether dams increased their body weight and fat deposition as a consequence of the AMH treatment (Supplementary Fig. 5a-c). We did not find any changes in body weight, subcutaneous fat mass or perigonadal fat mass in E19.5 dams injected for 3 days with vehicle, AMH or AMH + GnRH antag (Supplementary Fig. 5a-c).

Since P and E2 are vital to placental sufficiency and both hormones were greatly diminished in AMH-treated dams, we monitored whether there were any changes in litter loss, litter size and birthweights of pups when dams experienced diminished *Cyp19a1* and *Hsd3b1* expression (Supplementary Fig. 5d-f). We found a significant increase in the number of aborted embryos/litter and smaller litters when dams where treated with AMH as compared to vehicle- and AMH + GnRH antag-treated dams (Supplementary Fig. 5d-e). No changes in the body weights of pups at birth were detected (Supplementary Fig. 5f).

PAMH female offspring exhibit a masculinization of the brain

Perinatal gonadal steroids are primarily responsible for the sexual differentiation of the brain by triggering irreversible mechanisms25,26. We therefore analyzed whether the gestational AMH-dependent maternal hyperandrogenism might interfere with the establishment of brain sexual dimorphism in the offspring and contribute to the establishment of the adult PAMH phenotype. In mammals, gonadal T secretion occurs in a sexually dimorphic pattern with a male-specific neonatal T secretion (surge), which peaks in male mice during the first hours following birth (0-4 hours at P0)27,28. We therefore measured T levels 2 hours post-partum in control males and females as well as in PAMH female pups. This showed that T was markedly elevated in both control males and newborn PAMH females as compared to the control female pups (Fig. 4a). Interestingly, the neonatal T surge observed in PAMH female pups was completely prevented by the prenatal GnRH antagonist treatment (Fig. 4a). Similarly to T, a short-lived (1–12 h post-partum) surge in circulating LH is detected exclusively in newborn males in rodent as well as in primate species29. We thus measured serum LH in the pups and showed that LH was significantly more elevated in control male and PAMH female pups as compared to control females (Fig. 4a). Also in this case, the prenatal GnRH antagonist treatment prevented the LH neonatal surge of PAMH female pups (Fig. 4a).

To investigate whether the perinatal hyperandrogenism of the PAMH females could lead to long-term consequences in the organization of those brain areas, we analyzed three highly

steroid-sensitive features of well-known sexually dimorphic brain regions in adult control males (prenatal PBS-treated), control females (prenatal PBS-treated) and PAMH females (Fig. 4b, Supplementary Fig. 6). The established markers of developmental androgenization were the female-dominant tyrosine hydroxylase (TH) neuron population in the anteroventral periventricular nucleus (AVPV)30 and kisspeptin neuron population in the rostral periventricular area of the third ventricle (RP3V) of the hypothalamus31, and the male-dominant vasopressin (VP) expression in the bed nucleus of the stria terminalis (BnST) and the medial amygdaloid nucleus (MeA)32. As expected, we counted a higher number of TH neurons in the AVPV of control females versus control males (Fig. 4c) as well as a greater proportion of kisspeptin neurons in the RP3V of females versus male mice (Supplementary Fig. 6a,b). Importantly, PAMH female mice exhibited a male-like number of TH and kisspeptin cells in these regions (Fig. 4c and Supplementary Fig. 6a,b). A similar signature of androgenization was observed in the male-like VP expression in the BnST and MeA of PAMH females that displayed higher numbers of vasopressin-immunoreactive cells than control females, however without reaching the control male values (Fig. 4d).

These results show that PAMH female offspring exhibit a masculinization of both the neonatal T and LH surge, followed by a marked masculinization of the sexually dimorphic brain regions that regulate reproduction.

In utero exposure to excess AMH permanently alters the GnRH neuronal afferent network and the GnRH neuronal activity in the offspring

We next aimed at determining whether the marked hormonal and morphological signatures of androgenization detected in the PAMH animals were accompanied by protracted changes in GnRH neuronal morphology and electrical activity during adult life. Using *GnRH-GFP* mice and 3D-reconstruction analysis, we identified increased spine density both on the soma and along the primary dendrite (over the proximal 45 μm distance) in PAMH female mice compared with controls during diestrus (Fig. 5a-e). We also analyzed whether this increased spine density was correlated with increased Glutamatergic or GABAergic appositions. We found no significant differences in the number of appositions of vesicular glutamate transporter 2 (vGluT2)-immunoreactive (ir) puncta (associated with the primary dendrite of GnRH cells) in PAMH compared to control female mice (Supplementary Fig. 7a-c). However, when we counted the vesicular GABA Transporter (vGaT)-ir puncta on GnRH cell soma and proximal dendrite, we detected a significant increase in the number of vGaT appositions onto GnRH cells of PAMH compared to control, female diestrous mice (Fig. 5f-h). Although principally recognized as an inhibitory neurotransmitter in the adult brain, there is now a consensus that GABA is excitatory in adult GnRH neurons17,33. In order to test whether the elevated hypothalamic excitatory appositions onto GnRH neurons in PAMH animals effectively translates into increased neuronal activity, we performed whole-cell current-clamp recordings of GnRH-GFP neurons in acute coronal brain slices containing the preoptic area (POA). The recordings were done in animals sacrificed at diestrus, when GnRH secretion into the portal circulation is low (Fig. 5i-m). GnRH neurons from PAMH mice showed a robust, significant three-fold increase in their spontaneous action potential firing rate, as compared with controls (Fig. 5i-k). The average resting membrane potential (RMP) and average input resistance (R_{in}) of GnRH neurons were similar in control and

PAMH mice (Fig. 5l,m). Since R_{in} and the membrane capacitance (C_m) did not differ significantly among groups (mean ± s.e.m.; Control: 41.348 ± 5.121 pF, n = 6; PAMH: 39.893 ± 3.921 pF, n = 7; Student's *t*-test: $P = 0.823$, t = 0.229), we can assume that the change in GnRH neuronal firing in PAMH animals compared to control animals is not due to modifications of passive electrical membrane properties.

GnRH antagonist treatment of adult PAMH mice normalizes their neuroendocrine phenotype

Since our results uncovered a persistent hyperactivation of GnRH neurons in PAMH female animals, we reasoned that partially competing with natural GnRH for binding to membrane receptors on gonadotropes and thus decreasing the rate of LH and FSH release would ameliorate the PCOS-like phenotype observed in these mice. To assess this, we analyzed estrous cyclicity of adult PAMH female mice, over 90 days, before, during and after i.p. injections of increasing doses of GnRH antagonist (0.05 mg/Kg, 0.5 mg/Kg and 5 mg/Kg Cetrorelix acetate/per injection; Fig. 6a). We monitored daily vaginal cytology of PAMH animals throughout this time: before the beginning of the treatments, during the Cetrorelix administrations and during the recovery times (discontinuation of treatment; Fig. 6a). As shown in Figure 2, PAMH mice display prolonged time in metestrus/diestrus as compared to the control female offspring (Fig. 6a, grey areas). We initially monitored estrous cyclicity and LH concentrations in PAMH mice for 12 days before the beginning of Cetrorelix treatment to ascertain that the animals displayed the typical PCOS-like neuroendocrine alterations. Subsequently, to try attaining partial inhibition of GnRH receptor and normalize GnRH action on the pituitary, we injected mice i.p. every second day with Cetrorelix acetate at 0.05 mg/Kg for 12 days, followed by a recovery period (no treatment) and by 12 days treatment (every second day) with Cetrorelix acetate at 0.5 mg/Kg (Fig. 6a). Tail-blood samples were collected for LH measurements twice during the GnRH antagonist treatment and once during the 10 days recovery time that followed each administration period. To attain a complete blockade of GnRH receptor and suppression of LH secretion, we finally injected daily the same mice with 5 mg/Kg Cetrorelix acetate over 12 days (Fig. 6a).

As expected, PAMH mice were oligo-anovulatory, displaying about 25% of completed estrous cycles during 12 days as compared to control mice (Fig. 6b). Notably, normal estrous cyclicity was restored only when animals were injected with 0.5 mg/Kg of GnRH antagonist but not with the lowest or highest doses of the antagonist (0.05 mg/Kg and 5 mg/Kg Cetrorelix acetate; Fig. 6b). LH concentrations were also measured in PAMH and Control mice before the beginning of the treatments (Cetrorelix acetate for the PAMH group and PBS for the Control group), at day 2 and day 6, after the beginning of each treatment, and 4 days after the last injection (recovery time; Fig. 6c). The time-course and dose-effect experiments showed that the high mean LH values, initially observed in PAMH mice, were normalized following the intermittent GnRH antagonist treatment at the 0.5 mg/Kg dose only (Fig. 6c). Serum LH levels in PAMH mice following the injections with the lowest dose of Cetrorelix acetate (0.05 mg/Kg) were found to be significantly more elevated than in Control animals, whereas they were significantly suppressed when PAMH mice were treated daily with the highest dose at 5 mg/Kg (Fig. 6c). As in clinical practice, the effects of

Cetrorelix on LH secretion were reversible a few days after discontinuation of treatment, independently of the dosage used (Fig. 6c).

After having identified the concentration of the GnRH antagonist that corrected the serum LH levels and estrous cyclicity in adult PCOS-like animals, further experiments utilized PBS or Cetrorelix at 0.5 mg/Kg every 48 hrs (Fig. 6d-h). We found that Cetrorelix treatment restored the % of time that animals spent in each cycle stage (Fig. 6d) when compared to control and PAMH animals (Fig. 6d). The aberrant T and LH concentrations, and heightened LH pulsatility, typical of PAMH mice, were also normalized by the intermittent Cetrorelix treatment at 0.5 mg/Kg (Fig. 6e-g). Finally, the ovarian morphology of PAMH+GnRH antagonist mice was also restored as compared to PAMH animals, with PAMH+GnRH antagonist ovaries displaying more corpora lutea and antral follicles than the PAMH group (Fig. 6h).

These data show that postnatal GnRH antagonist treatment can rescue the major PCOS-like traits of PAMH mice: oligo-anovulation, hyperandrogenism, increased LH concentrations and LH pulsatility.

Discussion

Serum AMH levels have been shown to decrease with age both in healthy women and in women with PCOS, although they remain always 2- to 3-fold higher and elevated until 40 years of age in subjects with PCOS34. On the other hand, AMH levels were previously found to be very low during pregnancy in women without decreased fertility15,16 and it has been assumed that this would be also the case for PCOS individuals. Herein, we show for the first time that lean pregnant women with PCOS have significantly higher circulating AMH levels than pregnant women with normal fertility.

Most women with PCOS are hyperandrogenic during pregnancy14,35, yet the cause of this remains enigmatic. In this study, we found a positive relationship between AMH levels and hyperandrogenism in pregnant lean women with PCOS but not in obese PCOS subjects. It is not known whether a causal-relationship between AMH and T might exist during gestation in humans. Nevertheless, our results in mice demonstrate that AMH has a programming effect leading to gestational and perinatal hyperandrogenism and subsequent changes in the HPG axis and hormone levels of both the dams and the progeny.

We showed for the first time that peripherally injected AMH_C can access the maternal brain, at the level of the ME, and act centrally by inducing GnRH neuronal activation. Circumventricular organs, like the ME and the OVLT, contain fenestrated endothelial cells that allow the passage of molecules below 35 kDa36,37. Therefore, circulating AMH_C can have direct access to GnRH dendrites and terminals, which express AMHR2 both in mice and humans11, extending outside the BBB in the OVLT38 and the ME37, respectively.

Blood-borne bioactive AMH is generally presumed to be the cleaved AMH_C39; although recent studies suggested that human blood might predominantly contain proAMH and $AMH_{N,C}$40,41. Whether circulating $AMH_{N,C}$ undergoes further cleavage at the ME remains to be investigated. However, the fact that peripheral administration of either proAMH or

AMH_C leads to overlapping phenotypes in the offspring of treated dams supports the latter hypothesis.

Several animal models of PCOS rely on the prenatal administration of dihydrotestosterone (DHT) to induce the emergence of PCOS-like traits42,43. However, it should be noted that pregnant women do not have DHT in their circulation. Here, we have generated the most relevant PCOS mouse model, from a clinical perspective, as our model is based on an AMH-driven gestational hyperandrogenism, which is then responsible for the pathophysiological alterations leading to the acquisition of neuroendocrine and reproductive defects in the offspring. This fits well with previous studies demonstrating that gestational hyperandrogenism in monkeys, either occurring naturally or driven by T treatment, induces PCOS-like reproductive and metabolic traits in adulthood44,45.

Our findings highlight a novel pathophysiological mechanism whereby exposure to AMH excess during pregnancy leads to a cascade of alterations impacting the maternal brain, the ovaries and the placenta. This results in a strong elevation of maternal LH and T, and in a drop of P and E2. The maternal androgenization is most likely the result of a dual action of AMH on the dams' physiology: 1) a central action exacerbating GnRH/LH-driven ovarian steroidogenesis and 2) an AMH-driven inhibition of *Cyp19a1* and *Hsd3b1* expression in the placenta, leading to an increase in T bioavailability and a drop of circulating E2 and P levels, respectively (Supplementary Fig. 8). Since GnRH antagonism prevents diminished placental aromatase and *Hsd3b1* expression, we can speculate that these effects could be mediated by a LH/LHR action alone or in combination with AMH. These findings are in line with clinical investigations, which identified lower placental aromatase activity in women with PCOS46, which might be partly attributable to elevated levels of circulating AMH. The very low P and E2 levels detected in AMH-treated pregnant mice, most likely due to compromised placental function, could explain the higher incidence of aborted embryos observed in these animals as compared to controls (Supplementary Fig. 8). Interestingly, numerous clinical reports indicate that women with PCOS have an increased risk of poor pregnancy outcomes47 and lower maternal E2 levels than women without PCOS48.

Here, we also showed for the first time that the AMH-driven gestational hyperandrogenism triggers a masculinization of both the neonatal T and LH surge, followed by a marked masculinization of the sexually dimorphic brain regions regulating reproduction in female offspring (Supplementary Fig. 8). Importantly, the neonatal T and LH surges of PAMH female pups were corrected by prenatal GnRH antagonist administration, indicating that the neonatal consequences of the gestational AMH treatments are programmed *in utero* and not neonatally.

Since GnRH neurons do not express androgen receptor or estrogen receptor alpha (ERα)49, steroid hormone receptor activation are likely to occur in upstream neuronal afferents. We indeed provide evidence indicating that prenatal and neonatal hyperandrogenism leads to increased GABAergic appositions to GnRH neurons and to a persistent GnRH neuronal hyperactivity in adulthood. The alterations in vGaT, but not in vGluT2 appositions, observed in PAMH animals, phenocopy those of PNA mice17,19. This supports a modified afferent synaptic input to GnRH neurons, which includes an increased spine density associated not

with glutamatergic appositions but with increased GABAergic contacts. Since GABAergic inputs are known to excite GnRH neurons33,50, we can postulate that elevated excitatory innervation of GnRH neurons might be responsible for the increased GnRH/LH pulse frequency observed in PAMH adult females. Accordingly, most lean women with PCOS exhibit high-frequency LH secretion, which is suggestive of rapid GnRH pulsatility2,12. This is the case for 95% of the metabolically healthy women with PCOS women but not for obese patients with PCOS51–53. It should be noted that both the PNA mice17,18,54 and the PAMH animals, described in this study, did not present any weight alterations, indicating that these models are most representative of the "lean" PCOS condition. Such findings are highly consistent with our recently improved understanding of a leaner PCOS phenotype in the general population. Indeed, studies in referral PCOS populations (studied in the clinical environment) versus medically unselected populations have suggested that patients with PCOS diagnosed in the referral setting had a greater BMI and prevalence of obesity than women with PCOS detected in the medically unselected population 55–57. While it is clear that the weight of PAMH mice is unaffected, further study is needed to clarify whether other metabolic parameters known to be altered in hyperandrogenic lean women with PCOS58 such as glucose tolerance, insulin resistance or intra-abdominal fat storage, might be also altered in these animals.

In this study, we showed that the prenatal co-treatment of AMH with the GnRH antagonist prevented the appearance of PCOS-like neuroendocrine traits in the offspring, suggesting a critical role for GnRH in the prenatal programming of the disease. Our Nano-HPLC-HRMS analyses demonstrated that the peripherally-injected Cetrorelix (1.4 kDa) can access the maternal as well as the fetal brain. Notably, in rodents' ovaries, the expression of functional gonadotropin receptors starts at the end of the first week of life59,60 and therefore it is not yet in place at embryonic stages during which we treated the animals with AMH+GnRH antagonist. This evidence, together with our data showing that recombinant AMH cannot cross the placental barrier, strongly suggest that the effect of the prenatal GnRH antagonist treatment on the prevention of PCOS-like traits acquisition in the offspring is most likely occurring through the normalization of the maternal HPG axis.

Even more strikingly, we showed that intermittent delivery of Cetrorelix to adult PAMH mice, at a concentration that only partially competes with endogenous GnRH for binding to membrane receptors on gonadotropes, corrects their neuroendocrine and reproductive alterations. Given the fact that GnRH antagonists are frequently used in the clinic, with no adverse secondary effects, pharmacological antagonism aimed at tempering GnRH/LH secretion is an attractive therapeutic strategy to restore ovulation and fertility in individuals with PCOS characterized by normal body mass composition and high LH levels.

Online Methods

Study population: human patients

Blood samples were derived from the population-based Uppsala Biobank of Pregnant Women, where blood samples are collected in conjunction with routine ultrasound screening during gestational weeks 16-19. Gestational age was determined according to the ultrasound-based estimated date of birth. Eligible women were 18 years or older and without

blood-borne disease. In Sweden, all pregnant women are invited to a routine ultrasound examination, and approximately 97% of the pregnant population participate, hence, the Biobank subjects likely represent a population-based sample. Invitation to participate in the Biobank is random, with 70% of respondents accepting participation, it is estimated that the Biobank covers approximately half of the pregnant population of Uppsala County61. Upon inclusion, brief demographic data are collected, including ongoing chronic disorders, ongoing medication, smoking, height and weight. Following written informed consent, a plasma sample is collected. The sample was centrifuged within two hours and stored at -80°C.

By September 2013, 160 women with PCOS had donated a blood sample to the biobank, and from these blood samples, 32 normal-weight and 34 obese women with PCOS were selected for the present study based on their age (27-39 years old). PCOS was diagnosed according to Rotterdam criteria, i.e. presence of 2 of the following criteria: 1) polycystic ovaries on transvaginal ultrasound, 2) oligoamenorrhea 3) hyperandrogenism (either biochemical or clinical). Hyperandrogenism was defined as pre-pregnancy hyperandrogenism: either elevated testosterone, or elevated free androgen index (testosterone/sex hormone binding globulin > 0.05) or pre-pregnancy hirsutism as judged at the time of diagnosis. All women with PCOS had normal prolactin levels and thyroid function. Based on the initial, pre-pregnancy, diagnostic work-up, each woman was further phenotyped as hyperandrogenic PCOS (with signs of biochemical and/or clinical hyperandrogenism) or normoandrogenic PCOS. The medical records of all women with PCOS were scrutinized to ensure a correct diagnosis of PCOS, and to obtain information on obstetric and perinatal outcomes.

For each woman with PCOS an age- and BMI matched healthy control was chosen. Each control had donated blood samples during the same week as the respective case and were healthy according to the self-report. The medical records of the controls were reviewed to ensure than none had been diagnosed with PCOS or female factor infertility previously. Three blood samples from the controls could not be retrieved; hence 63 healthy controls were available for analysis. All women gave written informed consent for inclusion and the study has been approved by the Independent Ethical Review Board of Uppsala, Sweden.

AMH levels during pregnancy

Serum AMH levels were measured on samples stored at -80°C using the fully automated Acces Dxi sandwich immunoassay (B13127, Beckman Coulter). This assay measures the proAMH and the cleaved $AMH_{N,C}$ complex and uses recombinant human AMH as a calibrator. The limit of quantification of the assay is 0.57 pmol/L. Its intra- and inter-assay imprecision is < 5%. Results are expressed in pmol/L.

Animals

Timed-pregnant female wild-type C57BL/6J (B6) (Charles River, USA) and transgenic *Gnrh-Gfp*62 were group-housed under specific pathogen-free conditions in a temperature-controlled room (21-22°C) with a 12-h light/dark cycle and *ad libitum* access to food and water. Standard diet (9.5 mm Pelleted RM3, Special Diets Services, France) was given to all

mice during breeding, lactation and growth of young stock. Nutritional profile of the standard diet RM3 is the following: Protein 22.45%, Fat 4.2%, Fiber 4.42%, Ash 8%, Moisture 10%, Nitrogen free extract 50.4%; Calories: 3.6 kcal/gr.

Mice were randomly assigned to groups at the time of purchase or weaning to minimize any potential bias. No data sets were excluded from analyses.

C57BLl/6J *Gnrh-Gfp* transgenic mice have been previously characterized62. Animal studies were approved by the Institutional Ethics Committees of Care and Use of Experimental Animals of the University of Lille (France; Ethical protocol number: APAFIS#2617-2015110517317420 v5). All experiments were performed in accordance with the guidelines for animal use specified by the European Council Directive of 22 September 2010 (2010/63/EU). The sample size, sex and age of the animals used is specified in the text and/or figure legends.

Genotyping

Tail biopsies were used to isolate genomic DNA to identify the sex of embryos and mice at birth using Ube1 primers: Ube1 (forward), 5'CACCTGCACGTTGCCCTT-3' and Ube1 (reverse), 5'TGGATGGTGTGGCCAATG-3'. Males were identified with two bands marking both X (252 bp) and Y (334 bp) chromosomes and females with a single band representing only the X chromosome at 252 bp. *Gnrh-Gfp* transgenic animals were genotyped as previously described 62.

Prenatal anti-Müllerian Hormone (PAMH) treatment

Timed-pregnant adult (3-4 months) C57BL6/J (B6) dams were injected daily intraperitoneally (i.p.) from embryonic day (E) 16.5 to 18.5 with 200 μL of a solution containing respectively: 1) 0.01 M phosphate buffered saline (PBS, pH 7.4, prenatal control-treated), 2) PBS with 0.12 $mgKg^{-1}$/d human anti-Müllerian hormone (AMH) (AMH_C, R&D Systems, rhMIS 1737-MS-10, prenatal AMH (PAMH)-treated), 3) PBS with 0.12 $mgKg^{-1}$/d AMH and 0.5 $mgKg^{-1}$ of the GnRH antagonist, cetrorelix acetate (Sigma, Cat #C5249; PAMH + GnRH antag-treated), 4) 0.5 $mgKg^{-1}$/d of cetrorelix acetate in PBS (prenatal GnRH antag-treated), and 5) PBS with 0.12 $mgKg^{-1}$/d proAMH (Origene Technologies, Cat # TP308397; prenatal proAMH-treated, PproAMH).

Gnrh-Gfp adult females (P60-P90) were paired with males and checked for copulatory plugs, indicating day 1 of gestation. Pregnant *Gnrh-Gfp* dams were given either 200μl i.p. injections of PBS (control-treated) or 0.12 $mgKg^{-1}$/d AMHc in PBS from E16.5, E17.5 and E18.5. PAMH-*Gnrh-Gfp* and Control-*Gnrh-Gfp* offspring were weaned, genotyped and phenotyped during postnatal life.

Assessment of phenotype, estrous cycle and fertility

Control, PAMH, PAMH+GnRH antag, GnRH antag, and PproAMH female offspring were weaned at post-natal day P21 and checked for vaginal opening (VO) and time of first estrus. Anogenital distance (AGD) and body mass (grams, g) were measured at different ages during post-natal development (P30, 35, 40, 50 and 60). At VO and in adulthood (P60),

Europe PMC Funders Author Manuscripts

vaginal smears were performed daily for 16 consecutive days (4-cycles) for analysis of age of first estrus and estrous cyclicity. Vaginal cytology was analyzed under an inverted microscope to identify the specific day of the estrous cycle. The reproductive competency of these animals was determined by pairing the following mice: Control females mated with untreated C57BL6J (B6) wild-type males, PAMH females mated with PAMH males, PAMH +GnRH antag females mated with PAMH+GnRH antag males, and GnRH antag females mated with GnRH antag males for a period of 3 months. Unexperienced males and primiparous females, selected from at least three different litters, were used for the 90-days mating protocol test.

Number of pups/litter (number of pups), fertility index (number of litters per females over 3 months), and time to first litter (number of days to first litter after pairing) were quantified per treatment and pairing.

Postnatal GnRH antagonist treatment in PAMH mice and assessment of phenotype and hormone levels

PAMH adult female offspring were cycled for 12-days before GnRH antagonist treatments. Vaginal cytology was analyzed under an inverted microscope to record the specific day of the estrous cycle. Animals were injected intraperitoneally (i.p.) with 200μL of a solution containing 0.01M phosphate buffered saline (PBS, pH 7.4) with Cetrorelix acetate at 0.05 and 0.5 mg/Kg, every second day, or daily with Cetrorelix acetate at the dose of 5 mg/Kg. Tail-blood samples were collected for LH measurements twice before the beginning of the treatments, and at day 2 and 6 of each treatment as well as 4 days after the last injection (no treatment). Estrous cyclicity was monitored every day at the same time of day for the 12 days during postnatal GnRH antagonist treatments.

Ovarian histology

Ovaries were collected from 3-4-month-old diestrus mice, immersion-fixed in 4% PFA solution and stored at 4°C. Paraffin-embedded ovaries were sectioned at a thickness of 5 μm (histology facility, University of Lille 2, France) and stained with hematoxylin-eosin (Sigma Aldrich, Cat # GHS132, HT1103128). Sections were examined throughout the ovary. Total numbers of large antral follicles (containing a single large antrum), atretic and cysts-like follicles (large fluid-filled cysts with an attenuated granulosa cell layer, dispersed theca cell layer, and an oocyte lacking connection to the granulosa cells), and corpora lutea (CL) were classified and quantified as previously reported63. To avoid repetitive counting, each follicle was only counted in the section where the oocyte's nucleolus was visible. Using an ocular scale, follicles were classified by diameter into preantral, large growing (200–400 μm) and cystic follicles (> 400 μm). To avoid repetitive counting, CL were counted every 100 μm by comparing the section with the preceding and following sections. CL were characterized by a still present central cavity, filled with blood and follicular fluid remnants or by prominent polyhedral to round luteal cells.

Perfusions

Adult mice (P60-P90) were anesthetized with i.p. injections of 100 mg/kg of ketamine-HCl and 10 mg/kg xylazine-HCl and perfused transcardially with 20ml of saline, followed by

100 ml of 4% PFA in 0.1M phosphate buffer (PB) (4% PFA/0.1M PB; pH 7.6). Brains were collected, post-fixed in the same fixative for 2h at 4 °C, cryoprotected overnight in PB/Sucrose 30% at 4°C, embedded in OCT-embedding medium (Tissue-Tek), frozen and stored at -80°C until cryosectioning.

Immunohistochemistry

Tissues were cryosectioned coronally (Leica cryostat) at 35 μm for free-floating immunohistochemistry (IHC). Sections were blocked in an incubation solution of Tris-buffered saline (TBS 0.05M, pH 7.6), 0.25% bovine serum albumin (BSA; Sigma, A9418), 0.3% Triton X-100 (TBS-T; Sigma, T8787) with 10% normal donkey serum (NDS; D9663; Sigma) for 2h at room temperature before incubation with the following different primary antisera (depending on experiment) for 72h at 4°C: guinea pig anti-GnRH (EH#1018; 1:10,000)64,65, a generous gift from E. Hrabovszky (Laboratory of Endocrine Neurobiology, Institute of Experimental Medicine of the Hungarian Academy of Sciences, Budapest, Hungary), rabbit anti-GFP (Abcam ab6556; 1:1000), mouse monoclonal anti-vesicular GABA Transporter, vGaT) antibody (Synaptic Systems #131001; 1:500), guinea pig anti-vesicular glutamate transporter 2 (vGluT2) (Synaptic Systems #135404; 1:500), monoclonal mouse anti-Tyrosine Hydroxylase (TH) antibody (Millipore MAB318; 1:3000), guinea pig anti-(Arg^8)-Vasopressin (Peninsula Laboratories #T-5048; 1:2500), rabbit anti-cFos (Santa Cruz Biotechnology #sc-52; 1:5000), and a rabbit anti-kisspeptin (A. Caraty #566 1:10000, Institut National de la Recherche Agronomique)66. After TBS rinses, immunoreactivity (i.r) was revealed using the corresponding secondary antibodies (Life Technologies, Molecular Probes, Invitrogen) all 1:400, [Alexa-Fluor 488-conjugated #A21206; Alexa-Fluor 647-conjugated #A31573, #A31571; Alexa-Fluor 568-conjugated #A10042, #A10037] for 90 min in incubation solution at RT. After TBS washes, sections were incubated with 0.02% Hoechst (H3569; Invitrogen) in TBS-T for 15-mins at RT and mounted on gelatin-coated slides and coverslipped with mowiol medium (Sigma #81381).

Sections were examined using an Axio Imager. Z1 ApoTome microscope (Carl Zeiss, Germany) equipped with a motorized stage and an AxioCam MRm camera (Zeiss). For confocal observation and analyses, an inverted laser scanning Axio observer microscope (LSM 710, Zeiss) with an EC Plan NeoFluor ×100/1.4 numerical aperture oil-immersion objective (Zeiss) was used with an argon laser exciting at 488nm and helium laser exciting at 543nm (Imaging Core Facility of IFR114, of the University of Lille 2, France).

3D rendering and movies of GnRH neurons were generated using Imaris ×64 software (7.6.1, Bitplane).

Immunohistochemical analysis

Assessment of Fos-GnRH co-expression—Adult C57BL6/J (B6) females in diestrus were given i.p. injections of a solution containing 200 μL of 0.01M PBS, pH 7.4 or PBS with 0.12 $mgKg^{-1}/d$ AMH_C at 10:00. 90-min after injection, each mouse was anaesthetized and perfused transcardially as described above (*Perfusions*). Brains were collected, post-fixed in the same fixative for 2h at 4°C, embedded in OCT-embedding medium, frozen and

cryosectioned coronally (Leica cryostat) at 35 μm for free-floating IHC. Sections were processed for dual-label Fos-GnRH IHC.

Analysis of the double-labeled tissue was undertaken by counting the number of single-labeled and dual-labeled GnRH neurons in the preoptic area (POA: OVLT), with 2-3 brain sections representing the POA counted per mouse. Sections were scanned using a 20× objective to image Fos-GnRH double positively labelled cells for quantification. Activated neurons were identified as expressing Fos in the nucleus of the GnRH i.r. cell. The number of GnRH neurons co-expressing Fos was quantified and grouped to produce a mean percentage of the co-expression of GnRH-Fos in both PBS- and AMH-treated groups. The data from each mouse were then grouped to provide the median percentage ± interquartile range (IQR).

For the analysis of the total Fos-i.r cells in the POA, the same sections described above were examined using a 10 × objective. The total number of Fos positive cells per POA (OVLT) section in each treatment was quantified using the particle analysis program from Fiji (NIH); the total number of Fos-positive cells in the OVLT were quantified and averaged across OVLT sections from each animal and treatment.

Analysis of sexually dimorphic brain nuclei—For single-labeled Tyrosine Hydroxylase (TH) IHC, the number of TH-i.r cell bodies located within anteroventral periventricular nuclei were counted. For single-labeled Vasopressin (VP) IHC, the number of VP-i.r cell bodies located within the bed nucleus stria terminalis (BNST) and Medial Amygdala (MeA) were counted. For both TH and VP single-labeled IHC, each section containing the AVPV or the BNST and MeA were analyzed in each sex, mouse and treatment (3-5 sections per mouse). For single-labeled kisspeptin IHC, the number of kisspeptin-i.r cell bodies were counted in the rostral periventricular area of the third ventricle (RP3V), which comprises the anteroventral periventricular nucleus (AVPV) and the preoptic periventricular nucleus. Two brain sections at each level of the RP3V were analyzed per mouse, and the number of kisspeptin positive cells counted and combined to produce the mean number of kisspeptin neurons per section for the RP3V of each mouse.

The mean number of TH-, VP- and Kiss-i.r neurons counted per section for the sexually dimorphic brain regions of each mouse and treatment were then grouped to provide the mean ± s.e.m. values for the experimental groups.

Assessment of GnRH neuron spine density—Coronal brain sections from adult (P60-90) female Control-*Gnrh-Gfp* and PAMH-*Gnrh-Gfp* animals were analyzed for GnRH neuron spine density.

GFP-i.r GnRH neurons located within the rPOA were randomly chosen from adult (P60-P90) diestrus Control-*Gnrh-Gfp* ($n = 5$) and PAMH-*Gnrh-Gfp* female mice ($n = 5$) and were imaged using a LSM 710, Zeiss upright confocal laser scanning microscope equipped with LSM 710 software. For each GnRH-GFP cell, a stack of images at 0.25 μm intervals were collected using a 100× objective and 2× digital zoom function throughout the entire depth of the GFP-i.r neuron. Images containing the cell body and initial portion of the primary

dendrite were collected and soma and dendritic spine density were determined. Spines were identified as protrusions from the somata or dendrite and defined as being less than 5μm in length from the soma or proximal dendrite (the dendrite with the greatest circumference extending from the GnRH soma). GnRH neuron soma spine density was expressed as the number of spines per μm relative to the soma circumference. Spine density was quantified every 15 μm along the entire length of the proximal GnRH dendrite (0-45 μm) as 45 μm was the longest length of the proximal dendritic that could be imaged before the dendrite exited the section. Spine density was expressed as the number of spines/μm.

Analysis of vGaT or vGluT2 appositions on Gnrh-Gfp neurons—Coronal brain sections from adult (P60-90) female Control-*Gnrh-Gfp* and PAMH-*Gnrh-Gfp* animals were analyzed for GnRH neuron spine and vGaT or vGluT2 density. GFP/vGaT or GFP/vGluT2 double labeled neurons located within the rPOA from Control;*Gnrh-Gfp* and PAMH;*Gnrh-Gfp* adult (P60-P90) diestrus female mice were imaged using the same criteria above. A z-series stack of images using a 100× objective was generated to estimate the density of vGaT or vGluT2 appositions. A contact was defined when there were no black pixels between the primary *Gnrh-Gfp* dendritic spine and vGaT or vGluT2 positive terminals. For each image, the number of vGaT- or vGluT2-labeled puncta directly opposed to GFP-labeled neuronal soma and dendrite (up to 45 μm along the GnRH primary dendrite) were counted and combined to provide the mean values for each cell. The primary GFP-i.r dendrite could not be followed for more than 45 μm from the cell body, therefore we determined the number of vGaT appositions every 15 μm until the dendrite exited the section. Data are presented as vGaT or vGluT2 appositions/μm.

Fluorescent AMH assays

Recombinant bioactive AMH (AMH_C, R&D Systems, rhMIS 1737-MS-10) was tagged with a fluorescent dye (d2; MW: approx. 800 Da, max light output at 665nm) by Cisbio Bioassays (Codolet, France) as previously described for other hormones67–69. Fluorescently-labeled bioactive AMH (2.5 nmoles/animal; Cisbio Bioassays) was injected into the jugular vein of pregnant mice (E16.5), anesthetized with ketamine/xylazine, and mice sacrificed 2 min later. Dams' brains, fetal brains and placentae were collected and immersion-fixed in 4% PFA overnight at 4°C. Brains were cryoprotected overnight in PB/Sucrose 30% at 4°C, embedded in OCT-embedding medium, frozen and stored at -80°C until cryosectioning. Placentae were processed for iDisco tissue-clearing as described below.

Cetrorelix measurement in biological samples

Sample preparation for nano-HPLC-HRMS analysis—Timed-pregnant adult (3-4 months) C57BL6/J (B6) dams were injected daily i.p. from embryonic day (E) 16.5 to 18.5 with 200 μL of a solution containing respectively: 1) 0.01M phosphate buffered saline (PBS, pH 7.4, prenatal control-treated), 2) PBS with 0.5 $mgKg^{-1}$ of the GnRH antagonist, cetrorelix acetate (GnRH antag-treated). At E19.5, dams were anesthetized with ketamine/xylazine, and sacrificed by cervical dislocation. Dams' brains and fetal brains were collected, snap-frozen in liquid nitrogen and stored at -80°C until nano-HPLC-HRMS experiments. Murine maternal and embryo brain samples were prepared adapting the procedure described70. Briefly, brains were weighted, homogenized with 1% formic acid in

cold acetonitrile and incubated for 15 min at -20°C. After centrifugation, the supernatant was freeze-dried and reconstituted with 3% acetic acid and 1% trifluoroacetic acid (TFA). all solvents sourced from Sigma-Aldrich Merck. The reconstituted sample was purified with a solid phase extraction using a Phenomenex polymeric reversed phase cartridge (Strata-X 33µm Polymeric Reversed Phase, 60 mg/3mL, Phenomenex, Bologna, Italy). The cartridges were equilibrated with a methanol and water solution of acetic acid and TFA (96:3:1 v/v), loaded with sample, washed with a 70:30 solution of water solution with acetic acid and TFA (96:3:1 v/v) and methanol, and eluted with a 90:10 solution of methanol and 3% acetic acid. The eluted solution was gently dried under stream on nitrogen and reconstituted with 0.1% formic acid. When brains were homogenized, an internal standard (ganirelix, empirical formula $C_{80}H_{113}ClN_{18}O_{13}$) was added to obtain a final concentration of 100ng/ml.

Nano-HPLC-HRMS analysis parameters—A Dionex Ultimate 3000 (Thermo Scientific, Milan, Italy) nano-HPLC instrument coupled to a Orbitrap Fusion (Thermo Scientific, Milan, Italy) high resolution hybrid mass analyzer was used.

Seperation was achieved with an EASY-Spray PepMap® column (C18, 2 µm, 100Å, 75 µm × 500 mm, Thermo Scientific, Milan, Italy) using formic acid 0.1% in water (solvent A) and in acetonitrile:water 8:2 (solvent B) as mobile phases (ultrapure solvents for nano-LC, Sigma-Aldrich, Milan, Italy). The gradient conditions were as follow: 5% B for 5 min isocratic, up to 100% B in 30 min and reconditioned for at least 20 min. The first 5 minutes of isocratic flow was mandatory for the preconcentration step on a µ-precolumn (C18 PepMap 100, 300µm i.d. × 5 mm, Thermo Scientific, Milan, Italy), and water with 0.1% formic acid and 0.05% TFA. The injection volume was 1 µL and the flow rate 300 nL/min.

The column was equipped with a nanoESI source and the capillary voltage was 2000V in positive ion mode. The ion transfer tube temperature was 275°C and the pressure was standard (0.008 Torr). Full scan spectra were acquired in the range of *m/z* 350-2000. MS^n spectra were acquired in the range between the ion trap cut-off and precursor ion *m/z* values. CID collision energy was selected for each analyte to allow the survival of 5-10% of the chosen precursor ion. High resolution spectra were acquired with a resolution of 60000 (FWHM) and the mass accuracy of recorded ions (vs. calculated) was ± 5ppm units (without internal calibration).

Tissue clearing

We used iDisco clearing protocol, as previously described71. Samples were washed in PBS (twice for 1h), followed by 50% methanol in PBS (1h), 80% methanol (1h) and 100% methanol (2x 1h). Next, samples were bleached in ice cold 5% H_2O_2 in 20% DMSO/ methanol at 4°C overnight. Next, samples were washed in methanol (2x 1h), in 20% DMSO/ methanol (2x 1h), 80% methanol (1h), 50% methanol (1h), PBS (2x 1h), and stored in PBS at 4°C until processing. Samples were then incubated at RT on a rotating wheel at 12 rpm in a solution containing: 20% MeOH, 40% MeOH, 60% MeOH, 80% MethOH, 100% MeOH, 100% MeOH; 1h each. Delipidation was achieved with an overnight incubation in DCM/ Methanol (2:1), followed by a 30-min wash in 100% DCM (Dichloromethane; Sigma-Aldrich). Samples were cleared in dibenzylether (DBE; Sigma-Aldrich) for 2h at RT on

constant agitation and in the dark. Finally, samples were moved into fresh DBE and stored in glass tube in the dark and at RT until imaging. 3D imaging was performed as previously described72,73. An ultramicroscope (LaVision BioTec) using InspectorPro software (LaVision BioTec) was used to perform imaging. The light sheet was generated by a laser (wavelength 488 or 561 nm, Coherent Sapphire Laser, LaVision BioTec) and two cylindrical lenses. A binocular stereomicroscope (MXV10, Olympus) with a 2× objective (MVPLAPO, Olympus) was used at different magnifications (1.6×, 4×, 5×, and 6.3×). Samples were placed in an imaging reservoir made of 100% quartz (LaVision BioTec) filled with DBE and illuminated from the side by the laser light. A PCO Edge SCMOS CCD camera (2,560 × 2,160 pixel size, LaVision BioTec) was used to acquire images. The step size between each image was fixed at 2 μm.

Pulsatile LH measurements

Diestrus female adult mice were habituated with daily handling for 3–weeks. Blood samples (5μl) were taken from the tail at 10-min intervals for 2h (between 10:00 and 12:00) during diestrus, diluted in 45 μl PBS-Tween (0.05%) and immediately frozen and kept at -80°C. LH levels were determined by the previously described sensitive LH sandwich ELISA74. A 96-well high-affinity binding microplate (Corning) was coated with 50 μl of capture antibody (monoclonal antibody, anti-bovine LHβ subunit, 518B7; L. Sibley; University of California, UC Davis) at a final dilution of 1:1000 (in Na_2CO_3/$NaHCO_3$, 0.1M, pH 9.6) and incubated overnight at 4°C. Wells were incubated with 200 μl blocking buffer (5% (w/v) skim milk powder in 1 X PBS-T pH 7.4 [0.01M PBS, 0.05% Tween 20 (Sigma #P9416)] for 2hr at RT. A standard curve was generated using a two-fold serial dilution of mouse LH (reference preparation, AFP-5306A; National Institute of Diabetes and Digestive and Kidney Diseases National Hormone and Pituitary Program (NIDDK-NHPP) in 0.25% (w/v) BSA (Sigma, A9418) in PBS-T. The LH standards and blood samples were incubated with 50 μl of detection antibody (rabbit LH antiserum, AFP240580Rb; NIDDK-NHPP) at a final dilution of 1:10000 for 1.5h at RT. Each well containing bound substrate was incubated with 50 μl of horseradish peroxidase-conjugated antibody (goat anti-rabbit; Vector Laboratories, PI-1000) at a final dilution of 1:10000. After a 1.5h incubation, 100 μl 1-Step™ Ultra TMB-Elisa Substrate Solution (ThermoFisher Scientific, Cat #34028) was added to each well and left at RT for 10 min. The reaction was halted by the addition of 50 μl of 3M HCL to each well, and absorbance read at 490 nm. Pulses were confirmed using DynPeak75.

LH and T ELISA Assays

LH levels were determined by a sandwich ELISA, as described previously74, using the mouse LH–RP reference provided by A.F. Parlow (National Hormone and Pituitary Program, Torrance, CA). Plasma T levels were analyzed using a commercial ELISA (Demeditec Diagnostics, GmnH, DEV9911) 76 according to the manufacturers' instructions.

LH and T measurement in pregnant mice—Timed-pregnant female C57BL6/J (B6) dams were treated with i.p. injections of 200 μL of PBS or 0.12 $mgKg^{-1}$/d AMH in PBS from E16.5-E18.5. At E19.5, pregnant-treated dams were decapitated and trunk blood was harvested in sterile Eppendorf tubes and left on ice until centrifugation. Plasma was

collected after centrifugation of blood samples at 3000 *g* for 15 mins at 4°C and stored at -80° C until use. Mean T and LH levels were determined as described above.

LH and T measurement in P0 mice—Timed-pregnant C57BL6/J (B6) dams were given i.p injections of 200 μL PBS or 0.12 $mgKg^{-1}$/d AMH in PBS from E16.5-E18.5. Dams were allowed to deliver naturally. Pups were harvested 2h after birth. Tail biopsies of pups were taken to determine the sex of each animal (*see* Genotyping). Trunk blood and was collected from P0 males, control females and PAMH female pups for analysis of circulating testosterone and LH levels. Plasma was collected after centrifugation of blood samples at 3000 *g* for 15 mins at 4°C and stored at -80° C until use. T and LH levels were determined as described above.

Quantitative RT-PCR analyses

E19.5 placental tissue from female control and PAMH embryos was isolated for total RNA was using Trizol (ThermoFisher Scientific, Cat #15596026) and the RNeasy Lipid Tissue Mini Kit (Qiagen; Cat # 74804) using the manufacturer's instructions. For gene expression analyses, mRNAs obtained from E19.5 placental tissues were reverse transcribed using SuperScript® IV Reverse Transcriptase (Life Technologies). Real-time PCR was carried out on Applied Biosystems 7900HT Fast Real-Time PCR system using exon-boundary-specific TaqMan® Gene Expression Assays (Applied Biosystems): *Amhr2* (AMHR2-*Mm00513847_m1*); *Cyp19a1* (Cyp19a1-*Mm00484049_m1); Cyp11a1* (Cyp11a1-*Mm00490735_m1*); *Hsd3b1* (Hsd3b1-*Mm01261921_mH*); *Gnrh1* (Gnrh1-*Mm01315604_m1*); *Gnrhr* (Gnrhr-*Mm00439143_m1*); *Lhr* (Lhcgr-*Mm00442931_m1*). Control housekeeping genes*: ActB (*ActB-*Mm00607939_s1); Gapdh (*GAPDH-*Mm99999915_g1*).

Quantitative RT-PCR was performed using TaqMan® Low-Density Arrays (Applied Biosystems) on an Applied Biosystems thermocycler using the manufacturer's recommended cycling conditions. Gene expression data were analyzed using SDS 2.4.1 and Data Assist 3.01 software (Applied Biosystems), with *ActB* and *Gapdh* as control house-keeping mRNA following a standardized procedure. Values are expressed relative to control values, as appropriate, set at 1.

Brain slice electrophysiology preparation and recordings

Gnrh-Gfp adult females (3-4 months) were paired with adult *Gnrh-Gfp* males (3-4 months) and checked for copulatory plugs. Pregnant *Gnrh-Gfp* dams were given 200 μl i.p. injections of PBS or 0.12 $mgKg^{-1}$/d AMH in PBS on days 16.5, 17.5 and 18.5 of gestation. Adult (3-4 months) female diestrus Control;*Gnrh-Gfp* and PAMH;*Gnrh-Gfp* offspring were anaesthetized with isoflurane, and, after decapitation, the brain was rapidly removed and put in ice-cold oxygenated (O_2 95% / CO_2 5%) artificial cerebrospinal fluid (ACSF) containing the following (in mM): 120 NaCl, 3.2 KCl, 1 NaH_2PO_4, 26 $NaHCO_3$, 1 $MgCl_2$, 2 $CaCl_2$, 10 glucose, pH 7.4 (with O_2 95% / CO_2 5%). After removal of the cerebellum, the brain was glued and coronal slices (150μm thickness) were cut throughout the septum and preoptic area using a vibratome (VT1200S; Leica). Before recording, slices were incubated at 34ºC for a recovery period of 1h. After recovery, slices were placed in a submerged recording

chamber (32.8ºC; Warner Instruments) and continuously perfused (2ml/min) with oxygenated ACSF. *GFP*-positive GnRH neurons in the hypothalamic preoptic area were visually identified with a ×40 objective magnification in an upright Leica DM LFSA microscope under a FITC filter and their cell body observed by using IR-differential interference contrast. Whole-cell patch-clamp recordings were performed in current-clamp with bridge mode by using a Multiclamp 700B amplifier (Molecular Devices). Data were filtered at 1kHz and sampled at 5kHz with Digidata 1440A interface and pClamp 10 software (Molecular Devices). Pipettes (from borosilicate capillaries; World Precision Instruments) of resistance of 6-8 MΩ when filled with an internal solution containing the following (in mM): 140 K-gluconate, 10 KCl, 1 EGTA, 2 Mg-ATP and 10 HEPES, pH 7.3 with KOH. Bridge balance was adjusted to compensate for pipette resistance. All recordings were analyzed with Clampfit 10 (Molecular Devices). Junction potentials were determined to allow correction of membrane potential values. Electrical membrane properties were measured in current-clamp mode by applying a series of current pulses from – 60 to + 60 pA (1s, 10pA increments). Input resistance (R_{in}) was determined by measuring the slope of the linear portion of the current-voltage curve. Recordings were terminated if R_{in} changed more than 10% between the beginning and the end of the recording. Membrane capacitance (C_m) was calculated using the equation τ=RC, where τ=time constant, R=resistance, and C=capacitation. Membrane time constant was estimated by fitting a single exponential to the charging curve (Clampfit 10; Molecular Devices) generated from a hyperpolarizing current pulse (1s, 10pA) from rest.

Statistical analyses

All analyses were performed using Prism 7 (Graphpad Software, San Diego, CA) and assessed for normality (Shapiro–Wilk test) and variance, when appropriate. Sample sizes were chosen according to standard practice in the field. The investigators were not blinded to the group allocation during the experiments. However, analyses were performed by two independent investigators in a blinded fashion. For each experiment, replicates are described in the figure legends. No samples were excluded from the analyses.

For AMH measurement during pregnancy, as AMH levels were found not to be normally distributed in the study population, results are reported as median and 25^{th}-75^{th} percentile range. All comparisons between PCOS and control patients were performed using the nonparametric Mann-Whitney *U* test. The significance level was set at $P < 0.05$.

For animal studies, data were compared using an unpaired two-tailed Student's *t*-test or a one-way ANOVA for multiple comparisons followed by Tukey's multiple comparison *post-hoc* test. Data analyses for percentages were performed using either a Mann-Whitney *U* test (comparison between two experimental groups) or Kruskal-Wallis test (comparison between three or more experimental groups) followed by a Dunn's *post hoc* analysis. The number of biologically independent experiments, sample size, *P* values, age and sex of the animals are all indicated in the main text or figure legends. All experimental data are indicated as mean ± s.e.m or as the 25th–75th percentile, line at median. The significance level was set at $P < 0.05$.

Supplementary Material

Refer to Web version on PubMed Central for supplementary material.

Acknowledgments

We thank M. Tardivel (microscopy core facility), M.-H. Gevaert (histology core facility), D. Taillieu and J. Devassine (animal core facility) and the BICeL core facility of the Lille University School of Medicine for expert technical assistance. We are deeply indebted to Dr. Philippe Ciofi (U1215, Neurocentre Magendie, Institut National de la Santé et de la Recherche Médicale, Bordeaux, France) for his helpful feedback and discussion of the data. This work was supported by: the European Research Council (ERC) under the European Union's Horizon 2020 research and innovation program (ERC-2016-CoG to P.G. grant agreement n° 725149/REPRODAMH); the Institut National de la Santé et de la Recherche Médicale (INSERM), France [grant number U1172]; the Centre Hospitalier Régional Universitaire, CHU de Lille, France (Bonus H to P.G. and Ph.D. fellowship to N.E.H.M.); Agence Nationale de la Recherche (ANR), France [ANR-14-CE12-0015-01 RoSes and GnRH to P.G.]; Bourse France *L'Oréal-UNESCO Pour les Femmes et la Science* to B.K.T; Horizon 2020 Marie Sklodowska-Curie actions – European Research Fellowship (H2020-MSCA-IF-2014) to J.C.

References

1. Norman RJ, Dewailly D, Legro RS, Hickey TE. Polycystic ovary syndrome. Lancet. 2007; 370:685–697. [PubMed: 17720020]
2. Goodarzi MO, Dumesic DA, Chazenbalk G, Azziz R. Polycystic ovary syndrome: etiology, pathogenesis and diagnosis. Nature reviews. Endocrinology. 2011; 7:219–231.
3. Jayasena CN, Franks S. The management of patients with polycystic ovary syndrome. Nature reviews. Endocrinology. 2014; 10:624–636.
4. March WA, et al. The prevalence of polycystic ovary syndrome in a community sample assessed under contrasting diagnostic criteria. Human reproduction. 2010; 25:544–551. [PubMed: 19910321]
5. Wild RA, et al. Assessment of cardiovascular risk and prevention of cardiovascular disease in women with the polycystic ovary syndrome: a consensus statement by the Androgen Excess and Polycystic Ovary Syndrome (AE-PCOS) Society. The Journal of clinical endocrinology and metabolism. 2010; 95:2038–2049. [PubMed: 20375205]
6. Dumesic DA, Lobo RA. Cancer risk and PCOS. Steroids. 2013; 78:782–785. [PubMed: 23624028]
7. Cook CL, Siow Y, Brenner AG, Fallat ME. Relationship between serum mullerian-inhibiting substance and other reproductive hormones in untreated women with polycystic ovary syndrome and normal women. Fertility and sterility. 2002; 77:141–146. [PubMed: 11779604]
8. Pigny P, Jonard S, Robert Y, Dewailly D. Serum anti-Mullerian hormone as a surrogate for antral follicle count for definition of the polycystic ovary syndrome. The Journal of clinical endocrinology and metabolism. 2006; 91:941–945. [PubMed: 16368745]
9. Pellatt L, et al. Granulosa cell production of anti-Mullerian hormone is increased in polycystic ovaries. The Journal of clinical endocrinology and metabolism. 2007; 92:240–245. [PubMed: 17062765]
10. Pigny P, et al. Elevated serum level of anti-mullerian hormone in patients with polycystic ovary syndrome: relationship to the ovarian follicle excess and to the follicular arrest. The Journal of clinical endocrinology and metabolism. 2003; 88:5957–5962. [PubMed: 14671196]
11. Cimino I, et al. Novel role for anti-Mullerian hormone in the regulation of GnRH neuron excitability and hormone secretion. Nature communications. 2016; 7:10055.
12. Chang RJ. The reproductive phenotype in polycystic ovary syndrome. Nat Clin Pract Endocrinol Metab. 2007; 3:688–695. [PubMed: 17893687]
13. McAllister JM, Legro RS, Modi BP, Strauss JF 3rd. Functional genomics of PCOS: from GWAS to molecular mechanisms. Trends in endocrinology and metabolism: TEM. 2015; 26:118–124. [PubMed: 25600292]
14. Sir-Petermann T, et al. Early metabolic derangements in daughters of women with polycystic ovary syndrome. The Journal of clinical endocrinology and metabolism. 2007; 92:4637–4642. [PubMed: 17848407]

15. Koninger A, et al. Anti-Mullerian-hormone levels during pregnancy and postpartum. Reproductive biology and endocrinology : RB&E. 2013; 11:60. [PubMed: 23844593]
16. La Marca A, Giulini S, Orvieto R, De Leo V, Volpe A. Anti-Mullerian hormone concentrations in maternal serum during pregnancy. Human reproduction. 2005; 20:1569–1572. [PubMed: 15734752]
17. Sullivan SD, Moenter SM. Prenatal androgens alter GABAergic drive to gonadotropin-releasing hormone neurons: implications for a common fertility disorder. Proceedings of the National Academy of Sciences of the United States of America. 2004; 101:7129–7134. [PubMed: 15096602]
18. Moore AM, Prescott M, Campbell RE. Estradiol negative and positive feedback in a prenatal androgen-induced mouse model of polycystic ovarian syndrome. Endocrinology. 2013; 154:796–806. [PubMed: 23254197]
19. Moore AM, Prescott M, Marshall CJ, Yip SH, Campbell RE. Enhancement of a robust arcuate GABAergic input to gonadotropin-releasing hormone neurons in a model of polycystic ovarian syndrome. Proceedings of the National Academy of Sciences of the United States of America. 2015; 112:596–601. [PubMed: 25550522]
20. Orvis GD, Behringer RR. Cellular mechanisms of Mullerian duct formation in the mouse. Developmental biology. 2007; 306:493–504. [PubMed: 17467685]
21. Pinski J, et al. Chronic administration of the luteinizing hormone-releasing hormone (LHRH) antagonist cetrorelix decreases gonadotrope responsiveness and pituitary LHRH receptor messenger ribonucleic acid levels in rats. Endocrinology. 1996; 137:3430–3436. [PubMed: 8754771]
22. Halmos G, Schally AV, Pinski J, Vadillo-Buenfil M, Groot K. Down-regulation of pituitary receptors for luteinizing hormone-releasing hormone (LH-RH) in rats by LH-RH antagonist Cetrorelix. Proceedings of the National Academy of Sciences of the United States of America. 1996; 93:2398–2402. [PubMed: 8637885]
23. Duijkers IJ, et al. Single and multiple dose pharmacokinetics and pharmacodynamics of the gonadotrophin-releasing hormone antagonist Cetrorelix in healthy female volunteers. Human reproduction. 1998; 13:2392–2398. [PubMed: 9806255]
24. Novembri R, et al. Placenta expresses anti-Mullerian hormone and its receptor: Sex-related difference in fetal membranes. Placenta. 2015; 36:731–737. [PubMed: 25972076]
25. Simerly RB. Wired for reproduction: organization and development of sexually dimorphic circuits in the mammalian forebrain. Annu Rev Neurosci. 2002; 25:507–536. [PubMed: 12052919]
26. McCarthy MM, Arnold AP, Ball GF, Blaustein JD, De Vries GJ. Sex differences in the brain: the not so inconvenient truth. J Neurosci. 2012; 32:2241–2247. [PubMed: 22396398]
27. Corbier P, Edwards DA, Roffi J. The neonatal testosterone surge: a comparative study. Arch Int Physiol Biochim Biophys. 1992; 100:127–131. [PubMed: 1379488]
28. Clarkson J, Herbison AE. Hypothalamic control of the male neonatal testosterone surge. Philos Trans R Soc Lond B Biol Sci. 2016; 371 20150115.
29. Herbison AE. Control of puberty onset and fertility by gonadotropin-releasing hormone neurons. Nature reviews. Endocrinology. 2016; 12:452–466.
30. Simerly RB. Hormonal control of the development and regulation of tyrosine hydroxylase expression within a sexually dimorphic population of dopaminergic cells in the hypothalamus. Brain Res Mol Brain Res. 1989; 6:297–310. [PubMed: 2574404]
31. Clarkson J, Herbison AE. Postnatal development of kisspeptin neurons in mouse hypothalamus; sexual dimorphism and projections to gonadotropin-releasing hormone neurons. Endocrinology. 2006; 147:5817–5825. [PubMed: 16959837]
32. De Vries GJ, Panzica GC. Sexual differentiation of central vasopressin and vasotocin systems in vertebrates: different mechanisms, similar endpoints. Neuroscience. 2006; 138:947–955. [PubMed: 16310321]
33. Herbison AE, Moenter SM. Depolarising and hyperpolarising actions of GABA(A) receptor activation on gonadotrophin-releasing hormone neurones: towards an emerging consensus. Journal of neuroendocrinology. 2011; 23:557–569. [PubMed: 21518033]

34. Piltonen T, et al. Serum anti-Mullerian hormone levels remain high until late reproductive age and decrease during metformin therapy in women with polycystic ovary syndrome. Human reproduction. 2005; 20:1820–1826. [PubMed: 15802325]
35. Sir-Petermann T, et al. Maternal serum androgens in pregnant women with polycystic ovarian syndrome: possible implications in prenatal androgenization. Human reproduction. 2002; 17:2573–2579. [PubMed: 12351531]
36. Schaeffer M, et al. Rapid sensing of circulating ghrelin by hypothalamic appetite-modifying neurons. Proceedings of the National Academy of Sciences of the United States of America. 2013; 110:1512–1517. [PubMed: 23297228]
37. Prevot V, et al. The versatile tanycyte: a hypothalamic integrator of reproduction and energy metabolism. Endocrine reviews. 2018
38. Herde MK, Geist K, Campbell RE, Herbison AE. Gonadotropin-releasing hormone neurons extend complex highly branched dendritic trees outside the blood-brain barrier. Endocrinology. 2011; 152:3832–3841. [PubMed: 21791557]
39. Ragin RC, Donahoe PK, Kenneally MK, Ahmad MF, MacLaughlin DT. Human mullerian inhibiting substance: enhanced purification imparts biochemical stability and restores antiproliferative effects. Protein expression and purification. 1992; 3:236–245. [PubMed: 1392620]
40. Pankhurst MW, McLennan IS. Human blood contains both the uncleaved precursor of anti-Mullerian hormone and a complex of the NH2- and COOH-terminal peptides. American journal of physiology. Endocrinology and metabolism. 2013; 305:E1241–1247. [PubMed: 24045871]
41. Pankhurst MW, Chong YH, McLennan IS. Relative levels of the proprotein and cleavage-activated form of circulating human anti-Mullerian hormone are sexually dimorphic and variable during the life cycle. Physiol Rep. 2016; 4
42. Roland AV, Moenter SM. Reproductive neuroendocrine dysfunction in polycystic ovary syndrome: Insight from animal models. Frontiers in neuroendocrinology. 2014
43. Moore AM, Campbell RE. Polycystic ovary syndrome: Understanding the role of the brain. Frontiers in neuroendocrinology. 2017
44. Abbott DH, et al. Nonhuman primate models of polycystic ovary syndrome. Molecular and cellular endocrinology. 2013; 373:21–28. [PubMed: 23370180]
45. Abbott DH, et al. Clustering of PCOS-like traits in naturally hyperandrogenic female rhesus monkeys. Human reproduction. 2017; 32:923–936. [PubMed: 28333238]
46. Maliqueo M, et al. Placental steroidogenesis in pregnant women with polycystic ovary syndrome. European journal of obstetrics, gynecology, and reproductive biology. 2013; 166:151–155.
47. Katulski K, Czyzyk A, Podfigurna-Stopa A, Genazzani AR, Meczekalski B. Pregnancy complications in polycystic ovary syndrome patients. Gynecological endocrinology : the official journal of the International Society of Gynecological Endocrinology. 2015; 31:87–91. [PubMed: 25356655]
48. Maliqueo M, et al. Placental STAT3 signaling is activated in women with polycystic ovary syndrome. Human reproduction. 2015; 30:692–700. [PubMed: 25609240]
49. Huang X, Harlan RE. Absence of androgen receptors in LHRH immunoreactive neurons. Brain research. 1993; 624:309–311. [PubMed: 8252407]
50. DeFazio RA, Moenter SM. Estradiol feedback alters potassium currents and firing properties of gonadotropin-releasing hormone neurons. Molecular endocrinology. 2002; 16:2255–2265. [PubMed: 12351691]
51. Huang CC, et al. Symptom patterns and phenotypic subgrouping of women with polycystic ovary syndrome: association between endocrine characteristics and metabolic aberrations. Human reproduction. 2015; 30:937–946. [PubMed: 25662806]
52. Rebar R, et al. Characterization of the inappropriate gonadotropin secretion in polycystic ovary syndrome. The Journal of clinical investigation. 1976; 57:1320–1329. [PubMed: 770505]
53. Chang RJ, Mandel FP, Lu JK, Judd HL. Enhanced disparity of gonadotropin secretion by estrone in women with polycystic ovarian disease. The Journal of clinical endocrinology and metabolism. 1982; 54:490–494. [PubMed: 6799536]

54. Roland AV, Nunemaker CS, Keller SR, Moenter SM. Prenatal androgen exposure programs metabolic dysfunction in female mice. The Journal of endocrinology. 2010; 207:213–223. [PubMed: 20713501]
55. Azziz R. Introduction: Determinants of polycystic ovary syndrome. Fertility and sterility. 2016; 106:4–5. [PubMed: 27238627]
56. Lizneva D, et al. Phenotypes and body mass in women with polycystic ovary syndrome identified in referral versus unselected populations: systematic review and meta-analysis. Fertility and sterility. 2016; 106:1510–1520 e1512. [PubMed: 27530062]
57. Ezeh U, Yildiz BO, Azziz R. Referral bias in defining the phenotype and prevalence of obesity in polycystic ovary syndrome. The Journal of clinical endocrinology and metabolism. 2013; 98:E1088–1096. [PubMed: 23539721]
58. Dumesic DA, et al. Hyperandrogenism Accompanies Increased Intra-Abdominal Fat Storage in Normal Weight Polycystic Ovary Syndrome Women. The Journal of clinical endocrinology and metabolism. 2016; 101:4178–4188. [PubMed: 27571186]
59. McGee EA, Hsueh AJ. Initial and cyclic recruitment of ovarian follicles. Endocrine reviews. 2000; 21:200–214. [PubMed: 10782364]
60. Sokka T, Huhtaniemi I. Ontogeny of gonadotrophin receptors and gonadotrophin-stimulated cyclic AMP production in the neonatal rat ovary. The Journal of endocrinology. 1990; 127:297–303. [PubMed: 2174455]
61. Granfors M, et al. Thyroid testing and management of hypothyroidism during pregnancy: a population-based study. The Journal of clinical endocrinology and metabolism. 2013; 98:2687–2692. [PubMed: 23690313]
62. Spergel DJ, Kruth U, Hanley DF, Sprengel R, Seeburg PH. GABA- and glutamate-activated channels in green fluorescent protein-tagged gonadotropin-releasing hormone neurons in transgenic mice. J Neurosci. 1999; 19:2037–2050. [PubMed: 10066257]
63. Caldwell ASL, et al. Neuroendocrine androgen action is a key extraovarian mediator in the development of polycystic ovary syndrome. Proceedings of the National Academy of Sciences of the United States of America. 2017; 114:E3334–E3343. [PubMed: 28320971]
64. Hrabovszky E, et al. Sexual dimorphism of kisspeptin and neurokinin B immunoreactive neurons in the infundibular nucleus of aged men and women. Frontiers in endocrinology. 2011; 2:80. [PubMed: 22654828]
65. Casoni F, et al. Development of the neurons controlling fertility in humans: new insights from 3D imaging and transparent fetal brains. Development. 2016; 143:3969–3981. [PubMed: 27803058]
66. Clarkson J, et al. Sexual differentiation of the brain requires perinatal kisspeptin-GnRH neuron signaling. J Neurosci. 2014; 34:15297–15305. [PubMed: 25392497]
67. Balland E, et al. Hypothalamic tanycytes are an ERK-gated conduit for leptin into the brain. Cell metabolism. 2014; 19:293–301. [PubMed: 24506870]
68. Schaeffer M, et al. Rapid sensing of circulating ghrelin by hypothalamic appetite-modifying neurons. Proceedings of the National Academy of Sciences of the United States of America. 2013; 110:1512–1517. [PubMed: 23297228]
69. Xu C, et al. KLB, encoding beta-Klotho, is mutated in patients with congenital hypogonadotropic hypogonadism. EMBO Mol Med. 2017; 9:1379–1397. [PubMed: 28754744]
70. Wang H, Chung-Davidson YW, Li W. Identification and quantification of sea lamprey gonadotropin-releasing hormones by electrospray ionization tandem mass spectrometry. J Chromatogr A. 2014; 1345:98–106. [PubMed: 24768126]
71. Renier N, et al. iDISCO: a simple, rapid method to immunolabel large tissue samples for volume imaging. Cell. 2014; 159:896–910. [PubMed: 25417164]
72. Belle M, et al. Tridimensional Visualization and Analysis of Early Human Development. Cell. 2017; 169:161–173 e112. [PubMed: 28340341]
73. Belle M, et al. A simple method for 3D analysis of immunolabeled axonal tracts in a transparent nervous system. Cell reports. 2014; 9:1191–1201. [PubMed: 25456121]
74. Steyn FJ, et al. Development of a methodology for and assessment of pulsatile luteinizing hormone secretion in juvenile and adult male mice. Endocrinology. 2013; 154:4939–4945. [PubMed: 24092638]

75. Vidal A, Zhang Q, Medigue C, Fabre S, Clement F. DynPeak: an algorithm for pulse detection and frequency analysis in hormonal time series. PloS one. 2012; 7:e39001. [PubMed: 22802933]

76. Moore AM, Prescott M, Marshall CJ, Yip SH, Campbell RE. Enhancement of a robust arcuate GABAergic input to gonadotropin-releasing hormone neurons in a model of polycystic ovarian syndrome. Proceedings of the National Academy of Sciences of the United States of America. 2015; 112:596–601. [PubMed: 25550522]

Europe PMC Funders Author Manuscripts

Europe PMC Funders Author Manuscripts

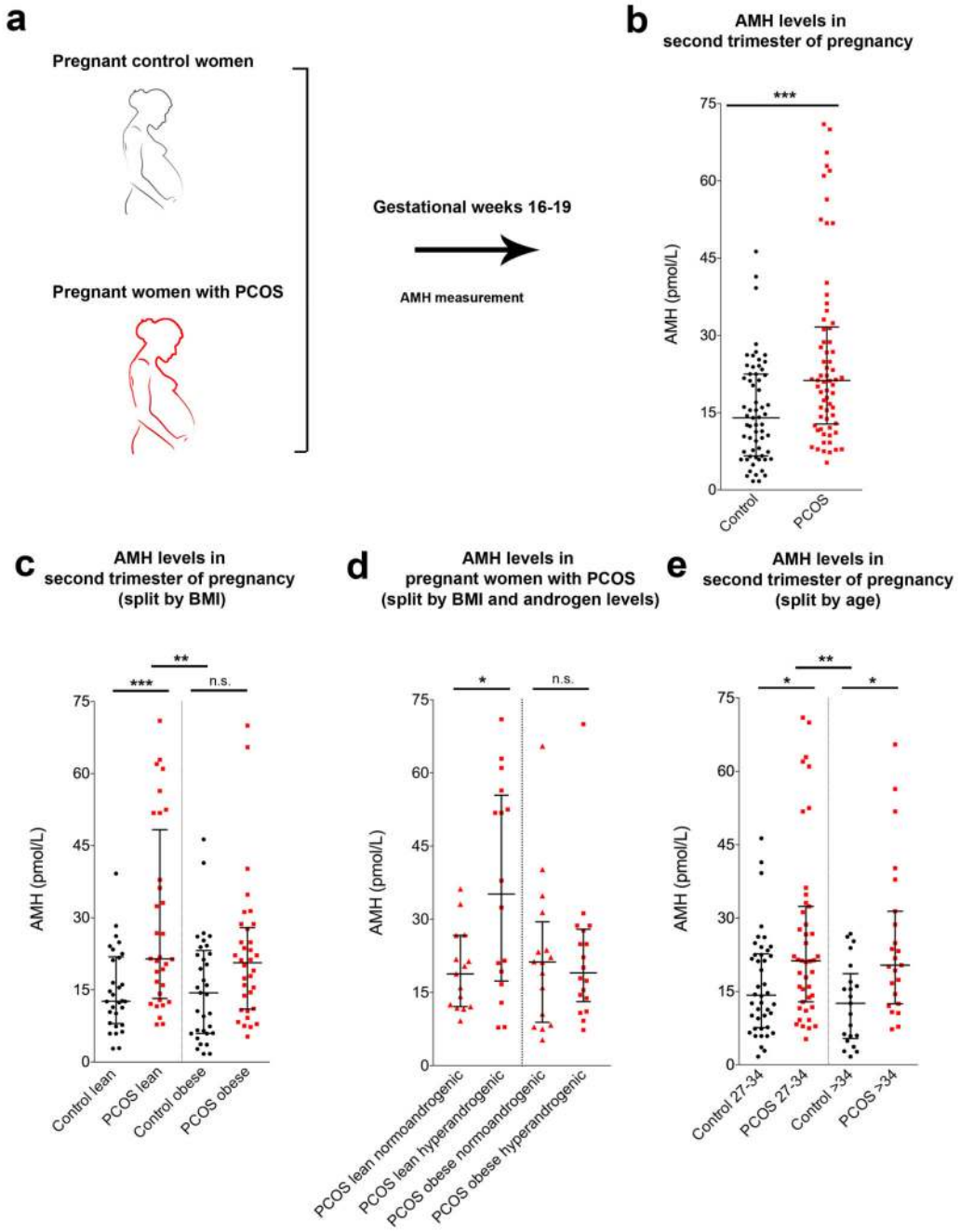

Figure 1. AMH levels during the second trimester of gestation are higher in women with PCOS than controls.

(**a**) Blood samples were derived from control and pregnant women with PCOS at gestational week 16-19 and AMH concentration was measured by ELISA. (**b**) Circulating AMH levels in control pregnant women ($n = 63$) and in pregnant women with PCOS ($n = 66$). Statistics by unpaired two-tailed Mann-Whitney U test, $^{***}P \leq 0.0001$. (**c**) Circulating AMH levels in control pregnant women and in pregnant individuals with PCOS stratified by their body mass index (BMI) and classified into lean (Control lean $n = 30$, PCOS lean $n = 32$) and

obese subjects (Control obese $n = 33$, PCOS obese $n = 34$). (**d**) Circulating AMH levels in pregnant women with PCOS stratified by their BMI and androgen levels (PCOS lean normoandrogenic $n = 15$, PCOS lean hyperandrogenic $n = 16$, PCOS obese normoandrogenic $n = 16$, PCOS obese hyperandrogenic $n = 18$). (**e**) Circulating AMH levels in control pregnant women and in PCOS pregnant subjects stratified by their age (Control 27-34 years old $n = 42$, PCOS 27-34 years old $n = 43$, Control > 34 years old $n = 21$, PCOS > 34 years old $n = 23$). The horizontal line in each plot corresponds to the median value from two technical replicates. The vertical line represents the 25^{th} – 75^{th} percentile range. Statistics in **c-e** were computed with one-way ANOVA (**c**: $F_{(3, 125)} = 7.534$, $P = 0.0001$; **d**: $F_{(3, 61)} = 3.922$, $P = 0.0126$; **e**: $F_{(3, 125)} = 6.282$, $P = 0.0005$) followed by Bonferroni *post hoc* test, * $P < 0.05$, ** $P \leq 0.005$, *** $P \leq 0.0005$; n.s. = not significant.

Europe PMC Funders Author Manuscripts

Europe PMC Funders Author Manuscripts

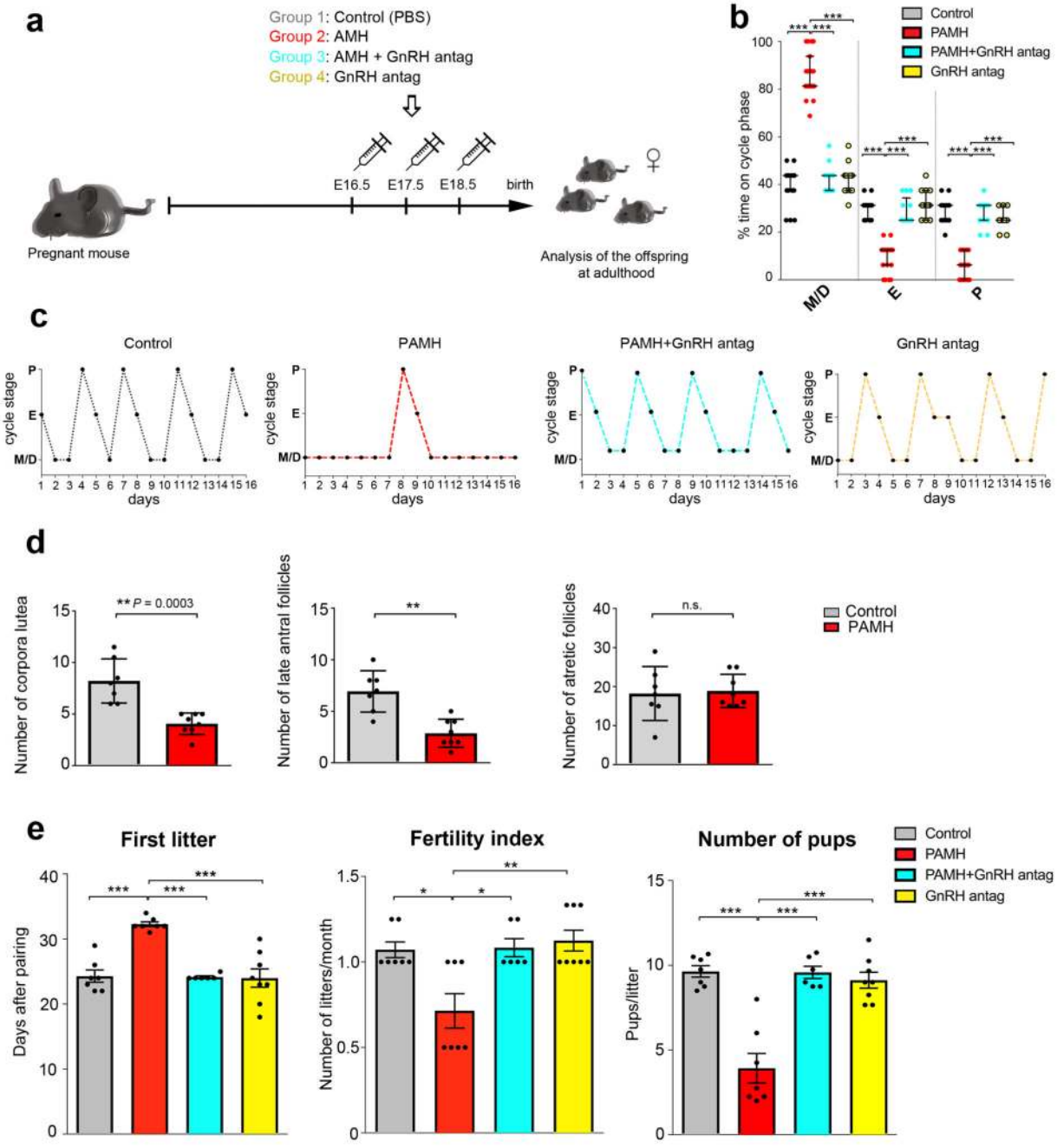

Figure 2. Prenatal AMH treatment disrupts estrous cyclicity, ovarian morphology and fertility in adult offspring.

(**a**) Schematic of experimental design whereby pregnant dams were subjected to different treatments of intraperitoneal (i.p.) injections during the late gestational period (embryonic days (E) 16.5 - E18.5). Pregnant dams (P90-P120; $n = 34$) were split into four treatment groups: PBS-treated ($n = 8$), AMH-treated (AMHc, $n = 10$), AMH+GnRH antag-treated (AMHc plus Cetrorelix acetate, $n = 8$), GnRH antagonist-treated (Cetrorelix acetate alone, 0.5 mg/Kg, $n = 8$). The offspring were designated as follows: Control, (PBS-treated); PAMH (Prenatal recombinant AMHc-treated); PAMH+GnRH antag, (PAMH plus Cetrorelix

acetate); GnRH antag (Cetrorelix acetate alone). (**b**) Quantitative analysis of ovarian cyclicity in adult (P60-P90) offspring mice (Control, $n = 15$; PAMH, $n = 19$; PAMH+GnRH antag, $n = 13$; GnRH antag, $n = 11$). Vaginal cytology was assessed for 16 days. The horizontal line in each scatter plot corresponds to the median value. The vertical line represents the 25^{th} – 75^{th} percentile range. Comparisons between treatment groups were performed using Kruskal-Wallis test followed by Dunn's *post hoc* analysis test; *** $P < 0.0001$. Data were combined from three independent experiments. (**c**) Representative estrous cyclicity of 10 mice/treatment group during 16 consecutive days. (**d**) Quantitative analysis of corpora lutea, late antral follicles and atretic follicles in the ovaries of Control ($n = 7$, age: P90) and PAMH mice ($n = 8$, age: P90). Statistics were performed with unpaired two-tailed Student's *t*-test (corpora lutea, $t_{(13)} = 4.879$, $^{**}P = 0.0003$; late antral follicles, $t_{(13)} = 4.637$, ** $P = 0.0005$; atretic follicles, $t_{(13)} = 0.226$, $P = 0.8243$, n.s. = not significant). Data are represented as mean ± s.e.m. and were combined from two independent experiments. (**e**) Fertility tests of the adult offspring mice (P90). Mating was performed for 90 days. Control females were paired with Control males ($n = 7$), PAMH females were paired with PAMH males ($n = 7$ for each sex), PAMH+GnRH antag females were paired with PAMH+GnRH antag males ($n = 6$ for each sex), and GnRH antag females were paired with GnRH antag males ($n = 8$ for each sex). Data are represented as mean ± s.e.m. Statistics in **e** were computed with one-way ANOVA (First litter, $F_{(3,24)} = 18.14$, $P < 0.0001$; Fertility Index, $F_{(3,24)} = 7.647$, $P = 0.0009$; Number of pups, $F_{(3,24)} = 24.26$, $P < 0.0001$) followed by Tukey's multiple comparison *post hoc* test, * $P < 0.05$, ** $P \leq 0.005$, *** $P \leq 0.0005$. Data of fertility tests were combined from two independent experiments.

Europe PMC Funders Author Manuscripts

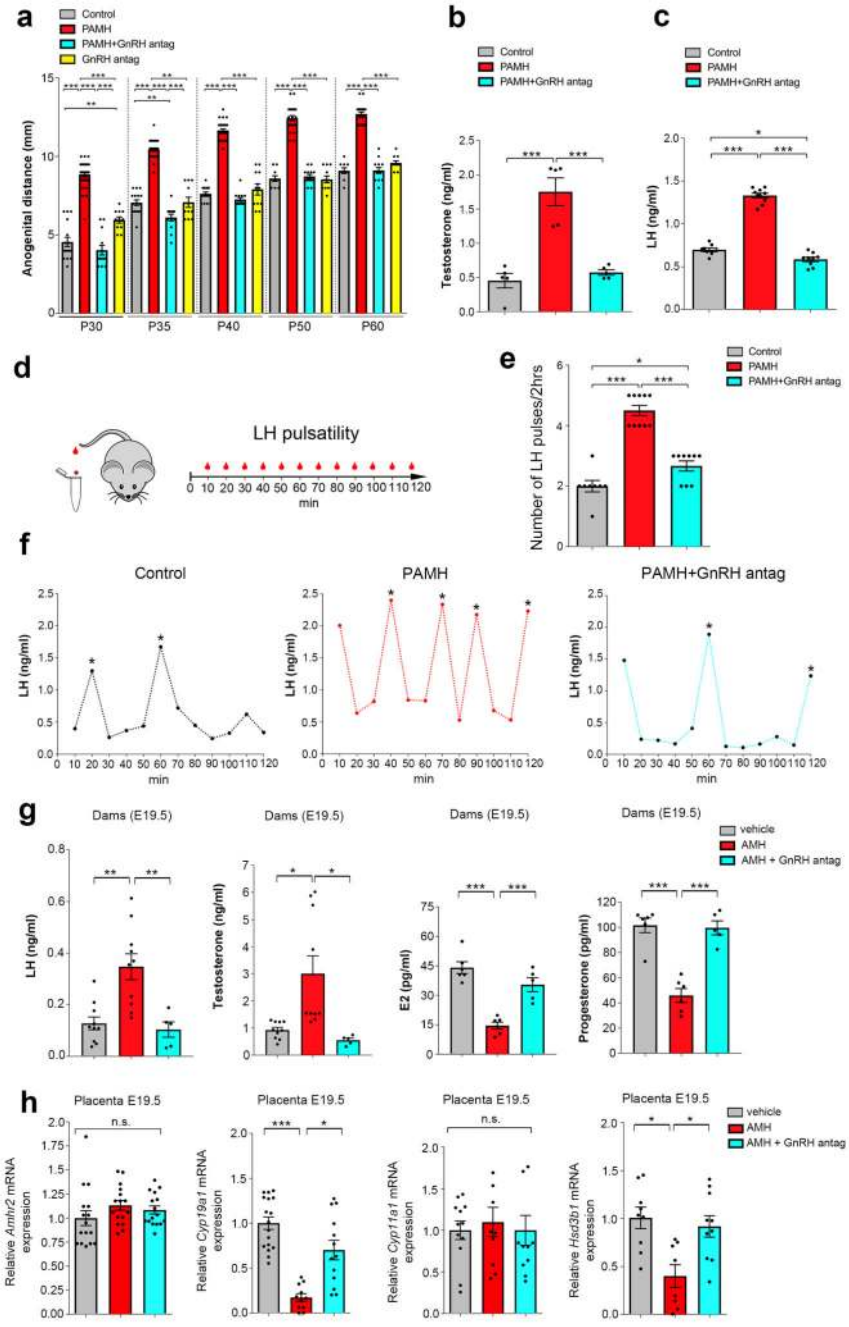

Figure 3. Prenatal AMH treatment leads to hyperandrogenism and elevation in LH secretion/ pulsatility.

(**a**) Anogenital distance (AGD) measured over post-natal days (P) indicated in female Control mice (P30, $n = 16$; P35, $n = 16$; P40, $n = 16$; P50, $n = 10$; P60, $n = 10$), PAMH mice (P30, $n = 29$; P35, $n = 32$; P40, $n = 32$; P50, $n = 24$; P60, $n = 24$), PAMH+GnRH antag mice ($n = 13$/age), and GnRH antag ($n = 11$/age) mice. Statistics were computed with one-way ANOVA (P30, $F_{(3,65)} = 108.2$, $P < 0.0001$; P35 $F_{(3,68)} = 155$, $P < 0.0001$; P40, $F_{(3,68)} = 234.5$, $P < 0.0001$; P50, $F_{(3,54)} = 143.4$, $P < 0.0001$; P60, $F_{(3,54)} = 165.4$, $P < 0.0001$) followed by Tukey's multiple comparison *post hoc* test. Data were pooled from 3

independent experiments. **(b)** Plasma testosterone concentration in adult females (P60) in diestrus: control group Control ($n = 5$), PAMH mice ($n = 5$) and PAMH+GnRH antag ($n = 5$) littermates. Statistics were computed with One-way ANOVA ($F_{(2,12)} = 28.67$, $P < 0.0001$), followed by Tukey's multiple comparison *post hoc* test. (**c**) Plasma LH levels in adult diestrous females (P60-P90). Number of mice: Control, $n = 8$; PAMH, $n = 10$; PAMH +GnRH antag, $n = 9$. One-way ANOVA ($F_{(2, 24)} = 257.3$, ***$P < 0.0001$), followed by Tukey's multiple comparison *post hoc* test. Data in **b** and **c** were combined from two independent replicates. (**d**) Schematic representation of tail-tip blood sampling in adult diestrous female mice (3-4 months old). (**e**) Number of LH pulses in adult (P60) diestrous females (Control, $n = 8$; PAMH, $n = 10$; PAMH+GnRH antag, $n = 9$). Statistics were computed with one-way ANOVA ($F_{(2,24)} = 57.06$, $P < 0.0001$) followed Tukey's multiple comparison *post hoc* test. Data were combined from three independent experiments. (**f**) Representative graphs for LH pulsatility of three independent experiments. Asterisks in (**f**) indicate the number of LH pulses/2-hr. (**g**) Hormone levels in trunk blood measured by ELISA at E19.5 in dams injected from E16.5 to E18.5 with either PBS (vehicle, $n = 9$-11), AMH ($n = 8$-10), AMH + GnRH antag ($n = 5$). Statistics were computed with one-way ANOVA (LH, $F_{(2,22)} = 11.48$, $P = 0.0004$; Testosterone, $F_{(2,22)} = 8.095$, $P = 0.0023$; Estradiol, E2, $F_{(2,14)} = 31.13$, $P < 0.0001$; Progesterone $F_{(2,14)} = 32.08$, $P < 0.0001$) followed by Tukey's multiple comparison *post hoc* test. Data were pooled from at least two independent experiments. Statistical significance in **a**, **b**, **c**, **e**, **g**: * $P < 0.05$, ** $P < 0.001$, *** $P = 0.0001$. (**h**) Real-time PCR analysis for *Amhr2*, *Cyp191a* (cytochrome P450 family 19, subfamily a, polypeptide 1), *Cyp11a1* (cytochrome P450, family 11, subfamily a, polypeptide 1), *Hsd3b1* (hydroxy-delta-5-steroid dehydrogenase, 3 beta- and steroid delta-isomerase 1) mRNA in the placenta of E19.5 dams. Dams were injected i.p. from E16.5 to E18.5 with either PBS (vehicle; *Amhr2*, $n = 16$; *Cyp191a*, $n = 17$; *Cyp11a1*, $n = 12$; *Hsd3b1*, $n = 9$), AMH (*Amhr2*, $n = 16$; *Cyp191a*, $n = 11$; *Cyp11a1*, $n = 9$; *Hsd3b1*, $n = 8$), or AMH + GnRH antag (*Amhr2*, $n = 16$; *Cyp191a*, $n = 13$; *Cyp11a1*, $n = 10$; *Hsd3b1*, $n = 10$). Comparisons between treatment groups were performed using Kruskal-Wallis test followed by Dunn's *post hoc* analysis test, *$P < 0.05$, ***$P < 0.0001$; n.s, not significant ($P > 0.05$). Data were combined from three independent experiments. Throughout the figure, data are displayed as mean ± s.e.m.

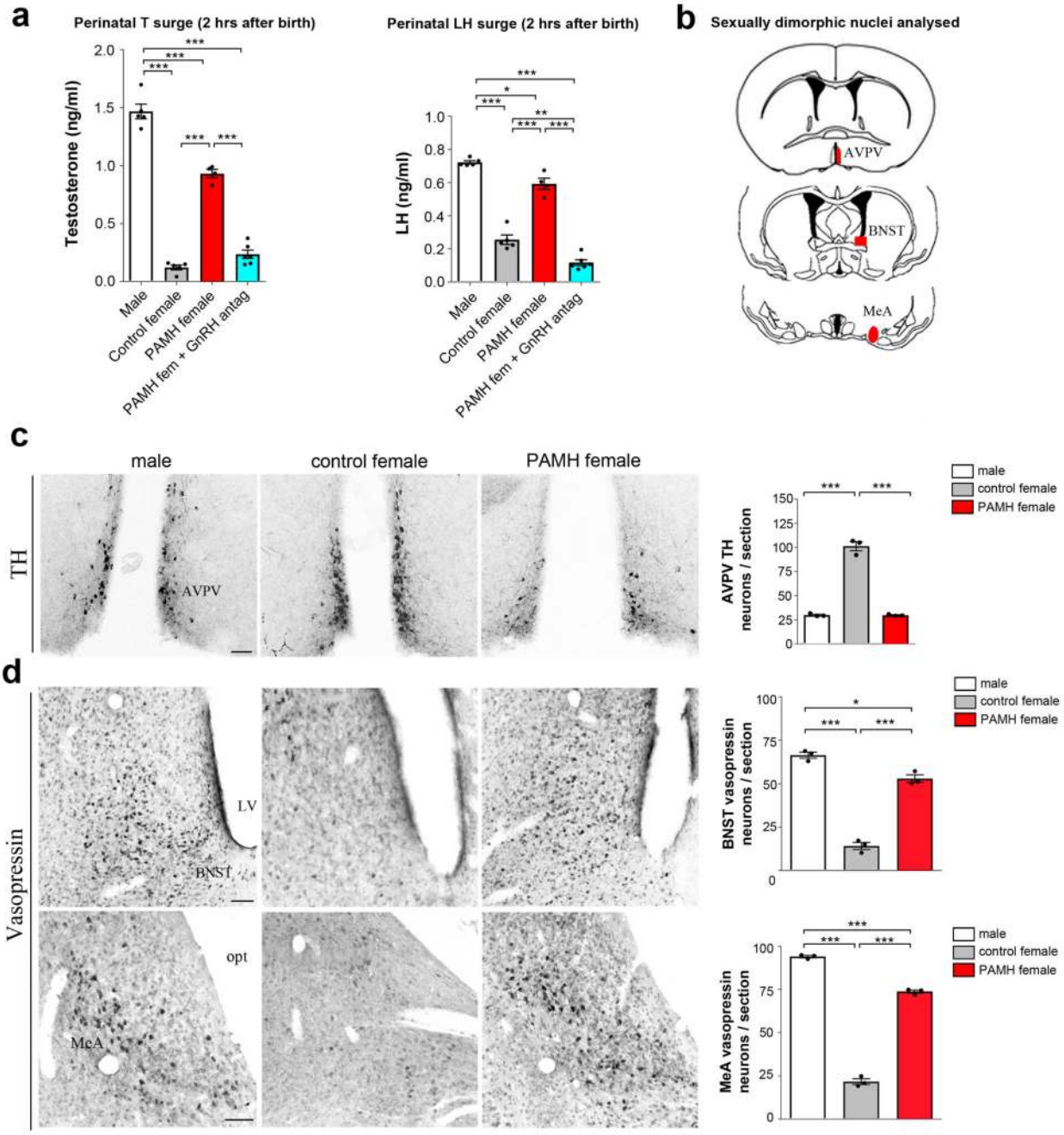

Figure 4. Prenatal AMH treatment increases perinatal T levels in females and masculinizes their brain.

(**a**) Plasma T and LH levels measured in pups 2 hours after birth (Males, $n = 5$; Control females, $n = 5$; PAMH females, $n = 4$; PAMH females + GnRH antag, $n = 6$). Statistics were computed with one-way ANOVA (Testosterone, $F_{(3, 16)} = 227.6$, $P < 0.0001$; LH, $F_{(3, 16)} = 163.3$, $P < 0.0001$) and Tukey's multiple comparison *post hoc* test. Error bars represent s.e.m. of three technical replicates. (**b**) Schematic representation depicting the analyzed sexual dimorphic neuroanatomical regions of the brain (denoted in red: anteroventral

Europe PMC Funders Author Manuscripts

Europe PMC Funders Author Manuscripts

periventricular nucleus, AVPV; bed nucleus of the stria terminalis, BNST; medial amygdala, MeA) expressing Vasopressin (VP) and Tyrosine Hydroxylase (TH). (**c**) Representative photomicrographs of three independent experiments showing TH-immunoreactive neurons in AVPV of a male, control female and PAMH female at P60. TH immunoreactive (-ir) neurons in the AVPV were quantified in these animal groups ($n = 3$ per sex and treatment). The number of AVPV TH-ir neurons are represented as the mean ± s.e.m. Statistics were computed with one-way ANOVA ($F_{(2,6)} = 231.1$, $P < 0.0001$) and Tukey's multiple comparisons *post-hoc* test. (**d**) Representative photomicrographs of three independent experiments showing VP-immunoreactive neurons in the BNST and MeA of a male, control female and PAMH female at P60. VP–ir neurons in the BNST and MeA were quantified in these animal groups ($n = 3$ per sex and treatment). Data are displayed as mean ± s.e.m. Statistics were computed with one-way ANOVA (BNST, $F_{(2,6)} = 185.2$, $P < 0.0001$; MeA, $F_{(2,6)} = 351.7$, $P < 0.0001$) followed by Tukey's multiple comparison *post hoc* test. Statistical significance in **a**, **c**, **d**: * $P < 0.05$, ** $P < 0.005$, *** $P < 0.0001$. Scale bars, 50 μm.

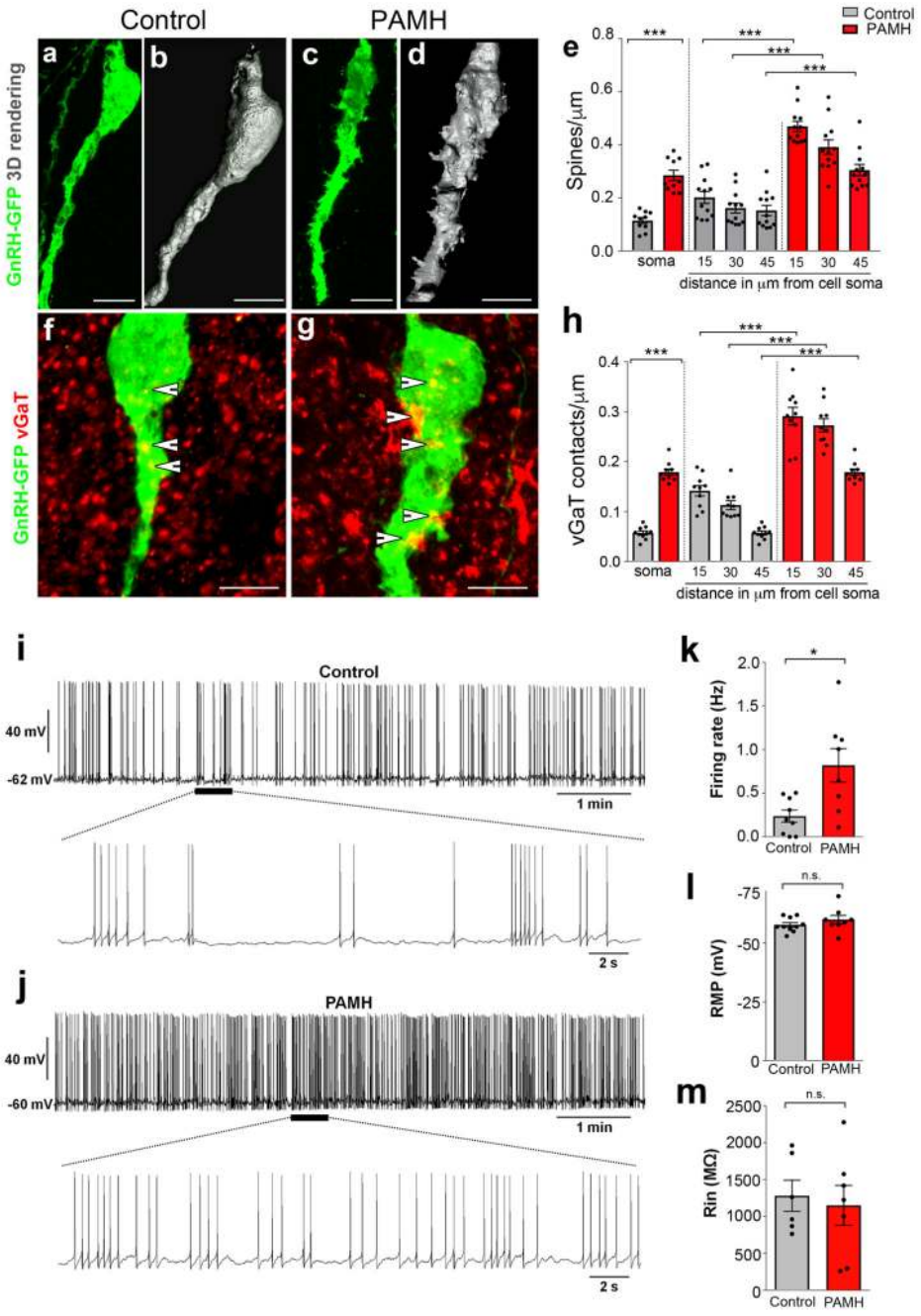

Figure 5. PAMH/*GnRH-GFP* mice exhibit higher GnRH dendritic spine density, increased GABAergic appositions to GnRH neurons and elevated firing frequency of GnRH neurons in adulthood.

(**a-d**) Representative projected confocal images and 3D reconstruction of three independent experiments showing *GnRH-GFP* neurons from an adult (P60) female diestrous control (**a, b**) and a PAMH (**c, d)** female diestrous mouse. (**e**) The GnRH dendritic spine density was analyzed in adult (P60) diestrous Control and PAMH/*GnRH-GFP* females. Spine density was quantified at the soma (Control, $n=10$ neurons from three animals; PAMH, $n=10$ neurons from three animals) and each 15 μm portion of the primary GnRH neuronal dendrite

Europe PMC Funders Author Manuscripts

(Control, n =12 neurons from three animals; PAMH, n =12 neurons from three animals). Statistics were performed with a paired two-tailed Student's t-test (soma, $t_{(18)} = 7.5434$, ***$P < 0.0001$; 15 μm from soma, $t_{(22)} = 9.08$, ***$P < 0.0001$; 30 μm from soma, $t_{(22)} = 6.92$, ***$P < 0.0001$; 45 μm from soma, $t_{(22)} = 5.252$, ***$P < 0.0001$). (**f, g**) Representative projected confocal images of three independent experiments showing a GFP-immunoreactive GnRH neuron (green) surrounded by vGaT-immunoreactive (red) puncta in an adult diestrous Control (**f**) and PAMH female mouse (**g**). Points where the vGaT signal was considered to be immediately adjacent to the GnRH neuron are indicated by arrowheads. (**h**) Quantification of the number of vGaT-immunoreactive puncta adjacent to GnRH neuron soma (Control, n =10 neurons from three animals; PAMH, n = 10 neurons from three animals) and along the primary GnRH neuronal dendrite is expressed as vGaT appositions/μm (Control, n =10 neurons from three animals; PAMH, n =10 neurons from three animals). Statistics were performed with a paired two-tailed Student's t-test (soma, $t_{(18)} = 16.4$, ***$P < 0.0001$; 15 μm from soma, $t_{(18)} = 7.341$; ***$P < 0.0001$, 30 μm from soma $t_{(18)} = 9.929$, ***$P < 0.0001$; 45 μm from soma; $t_{(18)} = 16.4$, ***$P < 0.0001$). (**i-m**) Spontaneous electrical activity and membrane properties of GnRH neurons recorded in acute brain slices from control and PAMH *GnRH-GFP* female diestrous mice. (**i**) Whole-cell current-clamp recording showing the typical spontaneous burst firing of a GnRH neuron from a control mouse. The bottom trace shows an expanded time scale of that recording. (**j**) Same experiment as in (**i**) but in a GnRH neuron from PAMH mouse. (**k**) Average firing rate of GnRH neurons recorded from Control (n = 9 cells from 4 animals, age P90-P120) and PAMH mice (n = 8 cells from 4 animals, age P90-P120). Statistics were performed with unpaired two-tailed Student's t-test ($t_{(15)} = 2.98$, *$P < 0.05$). (**l**) Average resting membrane potential (RMP) of GnRH neurons recorded from control (n =10 cells from 4 animals, age P90-P120) and PAMH mice (n = 8 cells from 4 animals, age P90-P120). Two-tailed Student's t-test, $t_{(16)} = 1.143$, $P = 0.27$, n.s. not significant. (**m**) Average input resistance (R_{in}) of GnRH neurons recorded from control (n = 6 cells from 4 animals, age P90-P120) and PAMH mice (n = 7 cells from 4 animals, age P90-P120). Unpaired two-tailed Student's t-test, $t_{(11)} = 0.3685$, $P = 0.7195$, n.s. not significant. Throughout, data are displayed as mean ± s.e.m. Experiments were replicated three times with comparable results. Scale bars, 50 μm.

Europe PMC Funders Author Manuscripts

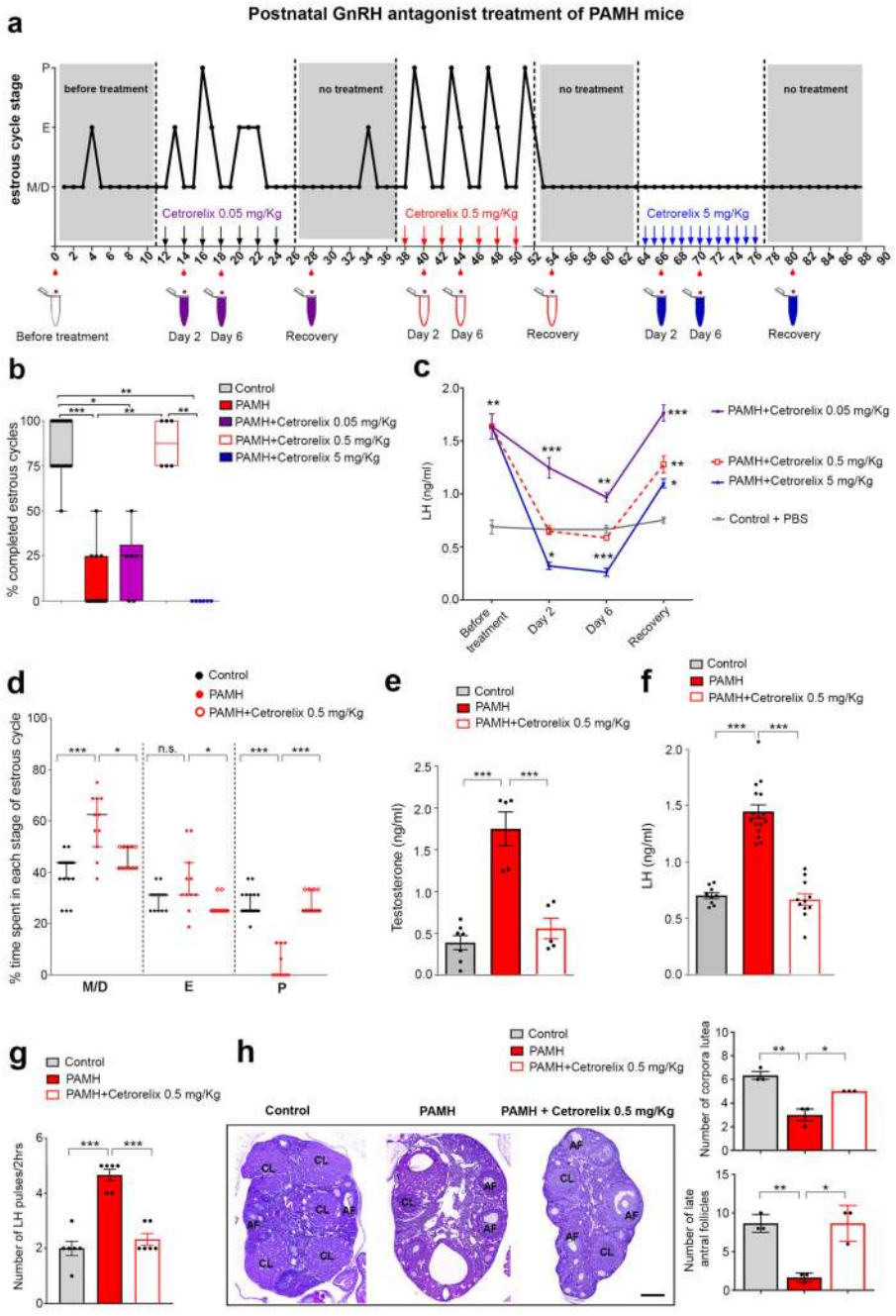

Figure 6. Postnatal GnRH antagonist treatment of PAMH mice restores the PCOS-like neuroendocrine phenotype.

(**a**) Schematic of experimental design whereby estrous cyclicity in PAMH adult mice was analyzed during 3 months, before and after postnatal intraperitoneal (i.p.) injections with 0.05, 0.5 and 5 mg/Kg Cetrorelix acetate. The Y axis refers to the different stages of the estrous cycle: Metaestrus/Diestrus (M/D), Estrus (E) and Proestrus (P). The X axis represents the time-course of the experiments (days). PAMH female mice (P60, $n = 6$) were injected i.p. for 12 days with Cetrorelix acetate at 0.05 mg/Kg (every second day) followed by Cetrorelix acetate at 0.5 mg/Kg (every second day) and finally by Cetrorelix acetate at 5

mg/Kg (every day). Tail-blood samples were collected for LH measurements twice before the beginning of the treatments, and at day 2 and 6 of each treatment as well as 4 days after the last injection (no treatment), that followed each administration period. (**b**) Quantitative analysis of the % of completed estrous cycles in Control (PBS-treated, $n = 19$), PAMH ($n = 13$), and PAMH mice ($n = 6$) postnatally treated with the three doses of GnRH antagonist (Cetrorelix 0.05 mg/Kg, Cetrorelix 0.5 mg/Kg, Cetrorelix 5 mg/Kg). The horizontal line in each scatter plot corresponds to the median value. The vertical line represents the 25^{th} – 75^{th} percentile range. Comparisons between treatment groups were performed using Kruskal-Wallis test followed by Dunn's *post hoc* analysis test. Data were combined from two independent experiments. (**c**) Time course of serum LH concentration in PAMH mice ($n = 6$) before the beginning of the treatment (day 0), 2 and 4 days after the first injection of each dose of Cetrorelix and after discontinuation of the drug (recovery time). Control animals (P60 females, $n = 3$) were injected with PBS and tail-blood was collected during the same temporal windows as for Cetrorelix treatment. Error bars represent s.e.m. from two independent experiments with two technical replicates each. Statistics were computed with one-way ANOVA (before treatment, $F_{(3,21)} = 10.6$, $P = 0.0004$; day 2, $F_{(3,21)} = 45.72$, $P < 0.0001$; day 6, $F_{(3,21)} = 67.10$, $P < 0.0001$, recovery, $F_{(3,21)} = 32.62$, $P < 0.0001$) followed by Bonferroni comparison *post hoc* test. (**d**) Percentage (%) of time spent in each estrous cycle in adult mice (Control or PAMH) injected for 12 days with either PBS or Cetrorelix at 0.5 mg/Kg every two days. The horizontal line in each scatter plot corresponds to the median value. The vertical line represents the 25^{th} – 75^{th} percentile range. The percentage (%) of time spent in each estrous cycle was quantified in Control ($n = 19$), PAMH ($n = 11$) and PAMH+Cetrorelix 0.5 mg/Kg ($n = 11$) mice (age: P60-P90). Comparisons between treatment groups were performed using Kruskal-Wallis test followed by Dunn's *post hoc* analysis test. Data were combined from three independent experiments. (**e**) Mean T levels measured in diestrus, at the end of the treatment time, in adult Control ($n = 7$), PAMH ($n = 5$) and PAMH+Cetrorelix-treated (0.5 mg/Kg; $n = 5$) animals. Statistics was computed with one-way ANOVA ($F_{(2,14)} = 29.24$, $P < 0.0001$) followed by Tukey's multiple comparison *post hoc* test. (**f**) Mean LH levels were measured in diestrus, at the end of the treatment time, in adult (P60-P120) Control mice ($n = 9$), PAMH ($n = 16$) and PAMH+Cetrorelix 0.5 mg/Kg ($n = 11$). Data were combined from three independent experiments. Statistics was computed with one-way ANOVA ($F_{(2,33)} = 72.2$, $P < 0.0001$) followed by Tukey's multiple comparison *post hoc* test. (**g**) LH pulsatility in adult (P90) diestrous females (Control, $n = 6$; PAMH, $n = 6$; PAMH+Cetrorelix 0.5 mg/Kg, $n = 6$). Statistics was computed with one-way ANOVA ($F_{(2,15)} = 40.71$, $P < 0.0001$) followed by Tukey's multiple comparison *post hoc* test. (**h**) Representative photomicrographs of ovaries stained with haematoxylin–eosin from adult (P60-P90) control, PAMH and Cetrorelix 0.5 mg/Kg mice ($n = 3$ each group). Right panels show the quantitative analyses for the mean number of corpora lutea (CL) and antral follicles (AF) in each treatment group. Comparisons between treatment groups were performed using one-way ANOVA (CL, $F_{(2,6)} = 23.38$, $P = 0.0015$; AF, $F_{(2,6)} = 21$, $P = 0.002$) followed by Tukey's multiple comparisons post-hoc test. Values in **e-h** are represented as the mean ± s.e.m. Statistical significance in **b-h**: * $P < 0.05$, ** $P < 0.005$, *** $P < 0.0001$; n.s., not significant ($P > 0.5$). Scale bars, 200 μm.